LS Scienza dei Materiali - a.a. 2005/06

Fisica delle Nanotecnologie – part 6

Version 4, Nov 2005
Francesco Fuso, tel 0502214305, 0502214293 - fuso@df.unipi.it
http://www.df.unipi.it/~fuso/dida

Isolated nanoparticles: clusters, mesoscopic structures, nanotubes

1/12/2005 – 16.30-18 – room T1

Introduction to the topic

Besides nanostructures anchored onto a substrate (e.g., useful in micro/nanoelectronics), **isolated nanoparticles** have widely been produced and investigated (e.g., for applications in **nanocomposites,** optics, mechanics, tribology, catalysis...)

Traditional name: **mesoscopic** structures, though their typical size lies far in the sub-micron range

Nanoclusters (atomic/molecular aggregates, either in the vapor phase, or dispersed on a substrate/in a matrix) are the first example

Isolated nanostructures with linear geometry (**nanowires, nanotubes**) can be produced as well by exploiting a variety of techniques

Typical mesoscopic behavior (e.g., electron transport) *in between* **bulk and purely quantum cofined systems (jumps across the two worlds are often observed)**

Typically strong influence of the large surface/volume ratio

Outlook

1. An extremely short introduction to clusters

2. Isolated nanoparticles with linear geometry: **nanowires** and applications

3. A few words on (polymer-based) **nanocomposites**

4. The amazing (?) world of carbon mesostructures (from fullerenes to nanotubes)

5. Mechanical properties of nanotube composites

6. Electronic structure, transport properties and nanoelectronic exploitations of carbon nanotubes

1. A few words on clusters and nanoparticles

Clusters: mesoscopic systems composed of a limited number of elemental components (typical mass ranging through 10^2 to 10^5)

Stable or metastable character ("**magic numbers**" for most favored configurations), frequently produced, observed and investigated in the **vapor** or liquid phase

Cluster physical chemistry deals mostly with fundamental issues (e.g., electronic configuration (quantum physics of a few body system)

Cluster experiments carried out mostly in the vapour phase

Whenever the cluster size increases, **nanoparticles** (stable, with the possibility to be **anchored onto a substrate or embedded in a matrix**) are produced with possible exploitations in several areas:
-Optics (*as we have already seen for metal nanoparticles*);
-Catalysis (*we will see an example);*
-"Mechanics" (e.g., lubrication, wear resistant coatings, tribology)

Fabrication includes also methods based on the liquid phase
Often nanoparticles are either dispersed on a surface or embedded in a matrix

Examples of fabrication methods for clusters/nanoparticles

Table 3.2. Methods for cluster generation

a) Condensation of atoms (supersaturation in vapor, liquids, solids)

Atoms produced by   heating: resistive, laser or electron beam
                    sputtering: by photon, atom, molecule, or ion impact, electric pulses, electric discharges

In beams	On surfaces	In matrices
Continuous:		
• gas aggregation	• atom deposition with subsequent surface diffusion	• co-evaporation of atoms with matrix material (matrix isolation)
• adiabatic expansion (with/without carrier gas)		
		• diffusion in/into matrix
• field emission (liquid-metal sources)	• soft landing	
		• photoreduction (photographic material)
• spraying techniques		
		• spraying techniques into liquid matrix (solvent extraction)
Pulsed:		
• laser vaporization		• chemical reduction in liquids (with or without nuclei): colloid generation metallorganic compounds: ligand shells
• pulsed nozzles for carrier gas		

b) Dispersion of bulk material or deposition

• sputtering	• cluster deposition from cluster beam	• co-evaporation of clusters with matrix material
• electric pulses, exploding wire	• nanocrystalline material by densification	• arc discharges in liquids
• arc discharges (Svedberg)		• pressing into porous matrix
		• chemical reduction in zeolites
• laser vaporization, ablation		• dispersion by ultrasound (emulsions)

Fabrication methods mostly based on vapor or liquid phase (physical and chemical)

Care to prevent self coalescence

2. Nanoparticles with a linear geometry: nanowires

Main motivations for producing, investigating, exploiting nanowires:

✓ Transport properties (1DEG-like)

✓ Mechanical properties (stress-strain, Young,..) enhanced by the cylindrical geometry (and affected by **quantum-like effects**

✓ Bulk/quantum-confined transition can often be seen

✓ In general, all properties are highly sensitive to the size and to the **external environment** (excellent sensors)
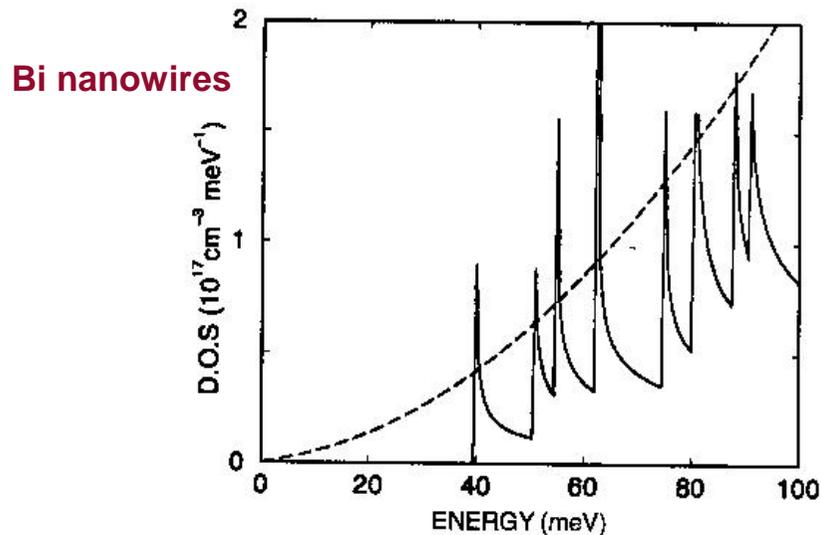
Bi nanowires

FIG. 15. Calculated effective densities of states for 40-nm bismuth nanowires (solid curve) and bulk bismuth (dashed curve). The zero energy refers to the band edge of bulk bismuth. The nonparabolic effects of the electron carriers are considered in these calculations.

1DEG behavior and the mesoscopic character can be jointly exploited in "sensitive" applications (especially, in semimetals)

Fabrication of isolated nanostructures with linear geometry (nanowires)
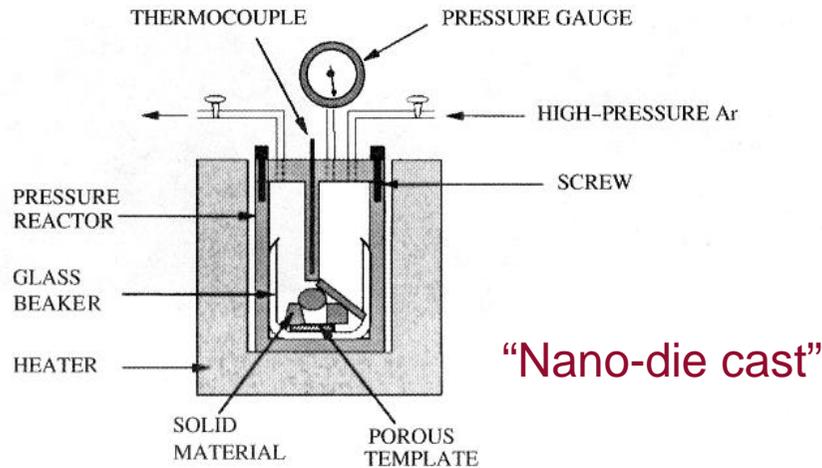

FIG. 5. Schematic of the experimental setup for the pressure injection of materials into the nanochannels of a porous template.
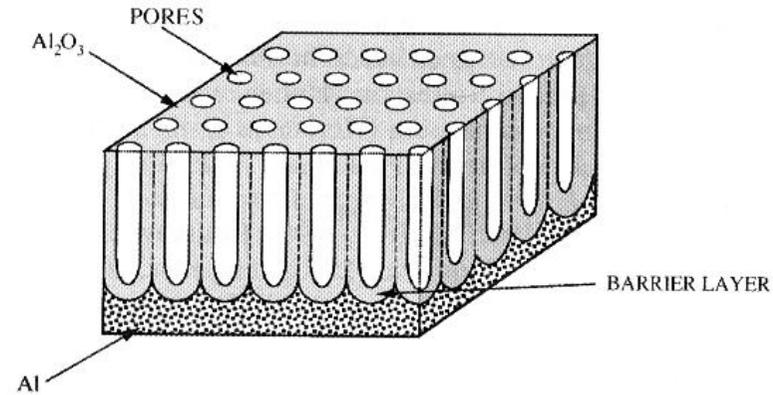
"Nano-die cast"

FIG. 1. Schematic of a porous anodic alumina template.

FIG. 2. SEM images of the top surfaces of porous anodic alumina templates anodized in (a) 4 wt% $H_2C_2O_4$ and (b) 20 wt% H_2SO_4. The average pore diameters in (a) and (b) are 44 nm and 18 nm, respectively.
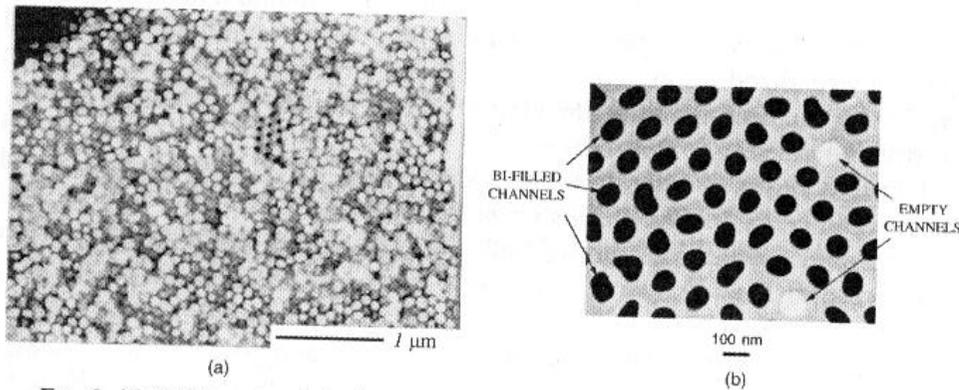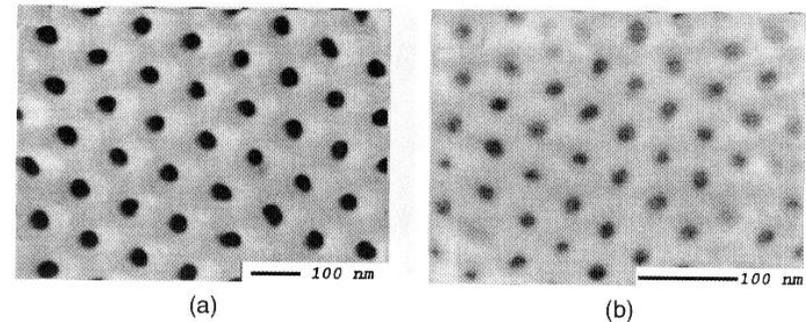

FIG. 6. (a) SEM image of the bottom surface of an anodic alumina template filled with bismuth. The pore diameter is 42 nm. (b) TEM micrograph of the cross section of a 65-nm bismuth nanowire array (Zhang et al., 1999).
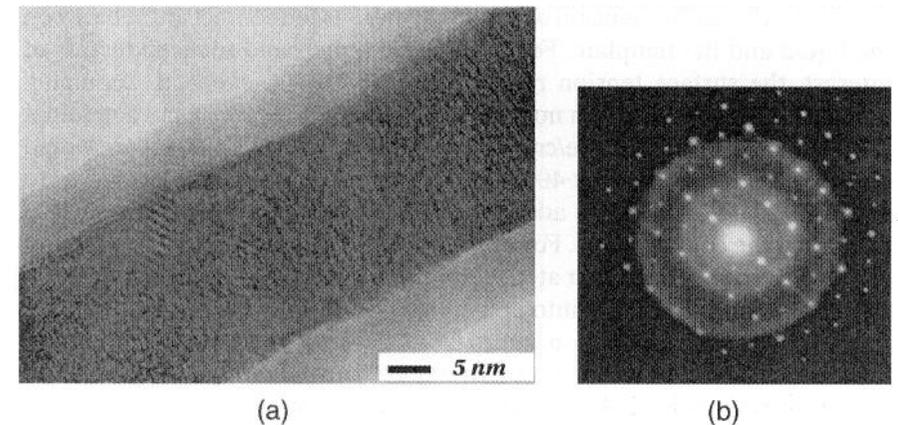

FIG. 7. (a) A HRTEM image of a 40-nm freestanding bismuth nanowire, showing lattice fringes. The amorphous surface layer is bismuth oxide formed upon air exposure of bismuth nanowire. (b) SAED pattern of a single Bi nanowire (Zhang et al., 1999).

Thermomechanical methods can be used to produce nanowires (with relatively large diameters) of materials having low melting points

Material	Growth Technique	Reference
Ag	DNA-template, redox	[4.23]
	template, pulsed ECD[a]	[4.24]
Au	template, ECD[a]	[4.25, 26]
Bi	stress-induced	[4.27]
	template, vapor-phase	[4.28]
	template, ECD[a]	[4.29], [4.30], [4.31]
	template, pressure-injection	[4.32], [4.16, 33]
Bi₂Te₃	template, dc ECD[a]	[4.34]
CdS	liquid-phase (surfactant), recrystallization	[4.35]
	template, ac ECD[a]	[4.36], [4.37]
CdSe	liquid-phase (surfactant), redox	[4.38]
	template, ac ECD[a]	[4.39], [4.40]
Cu	vapor deposition	[4.41]
	template, ECD[a]	[4.42]
Fe	template, ECD[c]	[4.15], [4.43]
	shadow deposition	[4.44]
GaN	template, CVD[c]	[4.45]
	VLS[b]	[4.46, 47]
GaAs	template, liquid/vapor OMCVD[d]	[4.48]
Ge	high-T, high-P liquid-phase, redox	[4.49]
	VLS[b]	[4.50]
	oxide-assisted	[4.51]
InAs	template, liquid/vapor OMCVD[d]	[4.48]
InP	VLS[b]	[4.52]
Mo	step decoration, ECD[a]+ redox	[4.53]
Ni	template, ECD[a]	[4.22], [4.31, 54]
PbSe	liquid phase	[4.55]
Pd	step decoration, ECD[a]	[4.56]
Se	liquid-phase, recrystallization	[4.57]
	template, pressure injection	[4.58]
Si	VLS[b]	[4.59]
	laser-ablation VLS[b]	[4.60]
	oxide-assisted	[4.61]
	low-T VLS[b]	[4.62]
Zn	template, vapor-phase	[4.63]
	template, ECD[a]	[4.64]
ZnO	VLS[b]	[4.65]
	template, ECD[a]	[4.64, 66]

a Electrochemical deposition
b Vapor-liquid-solid growth
c Chemical vapor deposition
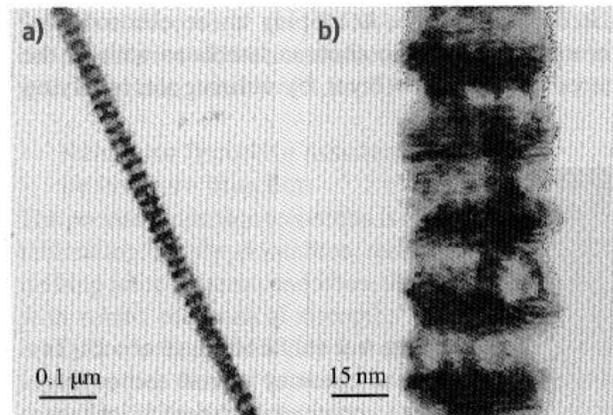d Organometallic chemical vapor deposition

Fig. 4.4 (a) TEM image of a single Co(10 nm)/Cu(10 nm) multilayered nanowire. (b) A selected region of the sample at high magnification [4.76]

Electrochemical Deposition

The electrochemical deposition technique has attracted increasing attention as an alternative method for fabricating nanowires. Traditionally, electrochemistry has been used to grow thin films on conducting surfaces. Since electrochemical growth is usually controllable in the direction normal to the substrate surface, this method can be readily extended to fabricate 1-D or 0-D nanostructures, if the deposition is confined within the pores of an appropriate template. In the electrochemical methods, a thin conducting metal film is first coated on one side of the porous membrane to serve as the cathode for electroplating. The length of the deposited nanowires can be controlled by varying the duration of the electroplating process. This

method has been used to synthesize a wide variety of nanowires e.g., metals (Bi [4.21, 29]; Co [4.73, 74]; Fe [4.15, 75]; Cu [4.20, 76]; Ni [4.22, 73]; Ag [4.24, 77]; Au [4.25, 26]); conducting polymers [4.7, 29]; superconductors (Pb [4.78]); semiconductors (CdS [4.37]); and even superlattice nanowires with A/B constituents (such as Cu/Co [4.20, 76]) have been synthesized electrochemically (see Table 4.1).

In the electrochemical deposition process, the chosen template has to be chemically stable in the electrolyte during the electrolysis process. Cracks and defects in the templates are detrimental to the nanowire growth, since the deposition processes primarily occur in the more accessible cracks, leaving most of the nanopores unfilled. Particle track-etched mica films or polymer membranes are typical templates used in the simple dc electrolysis. To use anodic aluminum oxide films in the dc electrochemical deposition, the insulating barrier layer that separates the pores from the bottom aluminum substrate has to be removed, and a metal film is then evaporated onto the back of the template membrane [4.79]. Compound nanowire arrays, such as Bi₂Te₃, have been fabricated in alumina templates with a high filling factor using the dc electrochemical deposition [4.34]. Figures 4.3a and b, respectively, show the top view and cross-sectional SEM images of a Bi₂Te₃ nanowire array [4.34]. The light areas are associated with Bi₂Te₃ nanowires, the dark regions denote empty pores, and the surrounding gray matrix is alumina.

Surfactants are also used with electrochemical deposition when necessary. For example, when using templates derived from PMMA/PS diblock copolymers (see above), methanol is used as a surfactant is used to facilitate pore filling [4.71], thereby achieving ∼ 100% filling factor.
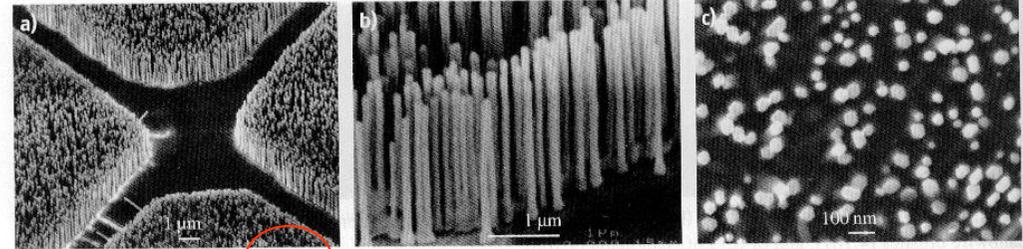
Different approaches can be combined (e.g., electroplating in the presence of a template)

Da B. Bhushan Ed., Springer Handbook of Nanotechnology (Springer, 2004)

Other methods for nanowire fabrication II
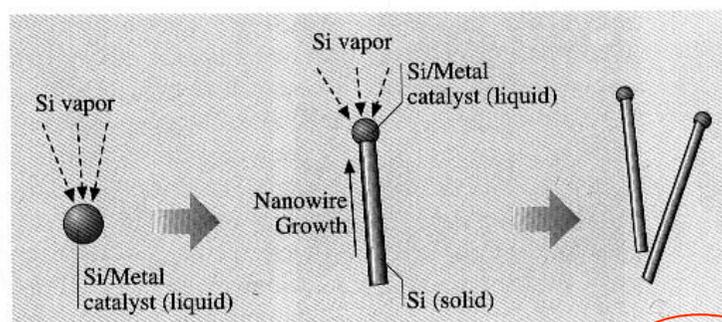
Fig. 4.5 Schematic diagram illustrating the growth of silicon nanowires by the VLS mechanism

4.1.2 VLS Method for Nanowire Synthesis

Some of the recent successful syntheses of semiconductor nanowires are based on the so-called vapor-liquid-solid (VLS) mechanism of anisotropic crystal growth. This mechanism was first proposed for the growth of single crystal silicon whiskers 100 nm to hundreds of microns in diameter [4.87]. The proposed growth mechanism (see Fig. 4.5) involves the absorption of source material from the gas phase into a liquid droplet of catalyst (a molten particle of gold on a silicon substrate in the original work [4.87]). Upon supersaturation of the liquid alloy, a nucleation event generates a solid precipitate of the source material. This seed serves as a preferred site for further deposition of material at the interface of the liquid droplet, promoting the elongation of the seed into a nanowire or a whisker, and suppressing further nucleation events on the same catalyst. Since the liquid droplet catalyzes the incorporation of material from the gas source to the growing crystal, the deposit grows anisotropically as a whisker whose diameter is dictated by the diameter of the liquid alloy

Fig. 4.11a–c SEM images of ZnO nanowire arrays grown on a sapphire substrate, where (a) shows patterned growth, (b) shows a higher resolution image of the parallel alignment of the nanowires, and (c) shows the faceted side-walls and the hexagonal cross section of the nanowires. For nanowire growth, the sapphire substrates were coated with a 1.0 to 3.5 nm thick patterned layer of Au as the catalyst, using a TEM grid as the shadow mask. These nanowires have been used for nanowire laser applications [4.115]

Fig. 4.6 (a) TEM images of Si nanowires produced after laser ablating a $Si_{0.9}Fe_{0.1}$ target. The dark spheres with a slightly larger diameter than the wires are solidified catalyst clusters [4.60]. (b) Diffraction contrast TEM image of a Si nanowire. The crystalline Si core appears darker than the amorphous oxide surface layer. The inset shows the convergent beam electron diffraction pattern recorded perpendicular to the wire axis, confirming the nanowire crystallinity [4.60]. (c) STEM image of $Si/Si_{1-x}Ge_x$ superlattice nanowires in the bright field mode. The scale bar is 500 nm [4.90]
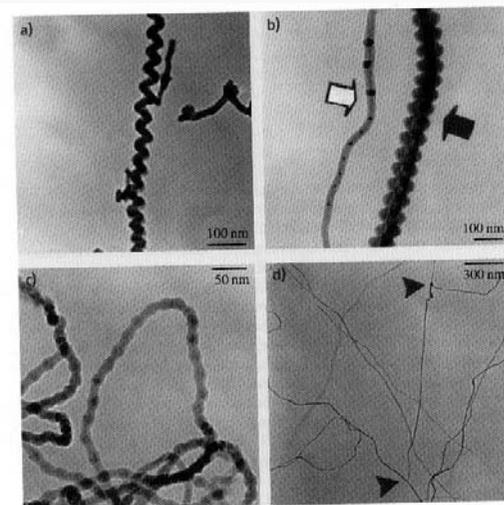
Fig. 4.13a–d TEM morphologies of four special forms of Si nanowires synthesized by the laser ablation of a Si powder target. (a) A spring-shaped Si nanowire; (b) fishbone-shaped (indicated by a solid arrow) and frog-egg-shaped (indicated by a hollow arrow) Si nanowires; and (c) pearl-shaped nanowires, while (d) shows poly-sites for the nucleation of silicon nanowires (indicated by arrows) [4.116]

Catalysis (by nanoparticles) can play a role in promoting growth of linear nanostructures
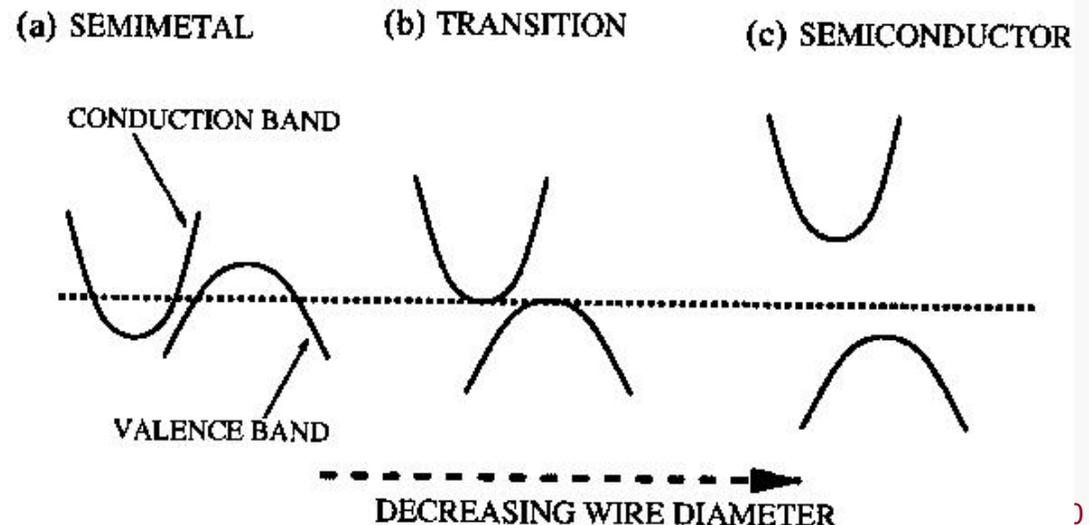
Properties and applications of nanowires I

For semimetals in bulk form, such as bismuth, the conduction band over-laps in energy with the valence band, and the electronic properties are governed by both the electrons and holes. In nanowires, the quantum con-finement effects cause the band edge of the electrons to move up in energy (see Fig. 16), whereas the valence band edge decreases in energy. The band-edge energies of electrons and holes shift in opposite directions in bismuth nanowires, decreasing the energy overlap between the conduction band and the valence band (Fig. 16). As the wire diameter continues to decrease, the energy overlap eventually vanishes (Fig. 16(b)), producing a band gap be-tween the lowest conduction subband and the highest valence subband. This semimetal-to-semiconductor transition will occur at a critical wire diame-ter d_c, which depends on the band overlap energy, the electron and hole effective masses, and the crystal orientation along the wire axis for the ma-terial of interest. The critical wire diameters for two group V semimetals, bismuth and antimony, are predicted to be about 50 nm and 10 nm (Lin et al., 2000c; Heremans et al., 2001), respectively. This quantum confinement–induced semimetal–semiconductor transition is one of the unique properties of nanowires made of semimetallic materials. Such a transition dramatically alters the electronic properties of nanowires, providing us with new possi-bilities for manipulating the band structures of materials.

Group V materials

By decreasing the wire transverse size, conduction and valence bands tend to lose their overlap (semimetal -> semiconductor)

FIG. 16. Schematic illustrating the semimetal–semiconductor transition in nanowires made of semimetals: (a) bulk semimetals with a band overlap between the electrons and the holes, (b) nanowires with the critical wire diameter d_c where the band overlap vanishes, and (c) nanowires with diameters smaller than d_c, exhibiting a bandgap between the conduction and valence bands.

(a) SEMIMETAL   (b) TRANSITION   (c) SEMICONDUCTOR

CONDUCTION BAND

VALENCE BAND

DECREASING WIRE DIAMETER

Ying, Nanostructured
Materials (Academic, 2001)

Due to the semimetal–semiconductor transition, the carrier concentration $N(T)$ of nanowires made of semimetallic materials is highly dependent on the wire diameter and temperature and must satisfy the condition $d_w \leq d_c$ to exhibit semiconducting behavior. As an example, Fig. 17 shows the calculated total carrier densities for various bismuth nanowires oriented along the $[01\bar{1}2]$ growth direction as a function of temperature (Lin *et al.*, 2000c). Three different types of temperature dependence for the carrier density are predicted for bismuth nanowires, depending on the wire diameters. For 10-nm bismuth nanowires, which are in the semiconducting regime, the carrier density increases exponentially with temperature. For 80-nm bismuth nanowires, which remain in the semimetallic regime for all temperatures, the carrier density is similar in temperature dependence to bulk bismuth. The lower carrier density of the 80-nm nanowires compared to bulk bismuth is due to the smaller band overlap in the former. For the 40-nm bismuth nanowires, the carrier density has a temperature dependence similar to bulk bismuth at high temperatures, but it drops rapidly with decreasing temperature at low temperatures. Because the carrier density is highly dependent on wire diameter, the transport properties of bismuth nanowires are expected to be highly sensitive to wire diameter, as will be shown experimentally in the section "temperature-dependent resistivity of nanowires."

FIG. 17. Calculated total carrier density (electrons and holes) as a function of temperature for bulk 3D bismuth and bismuth nanowires of different diameters oriented along the $[01\bar{1}2]$ direction.
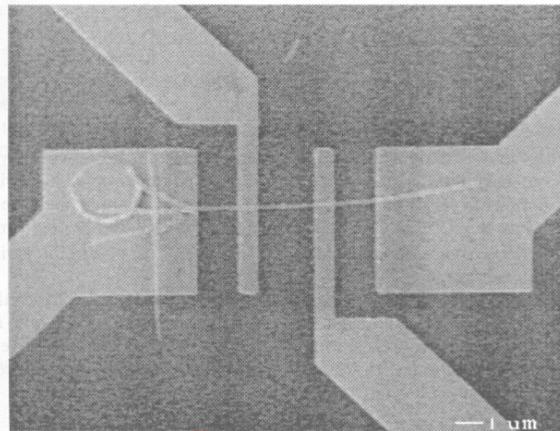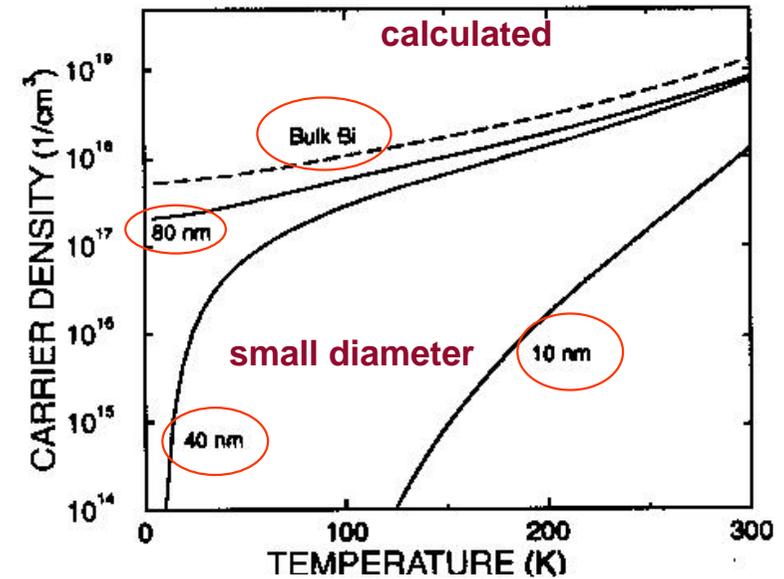

FIG. 18. SEM image of a 70-nm bismuth nanowire with four electrodes attached to the nanowire. The circle on the large left electrode is a reference point used to find the nanowire and to attach electrodes to it by a lithographic process (Cronin *et al.*, 1999).
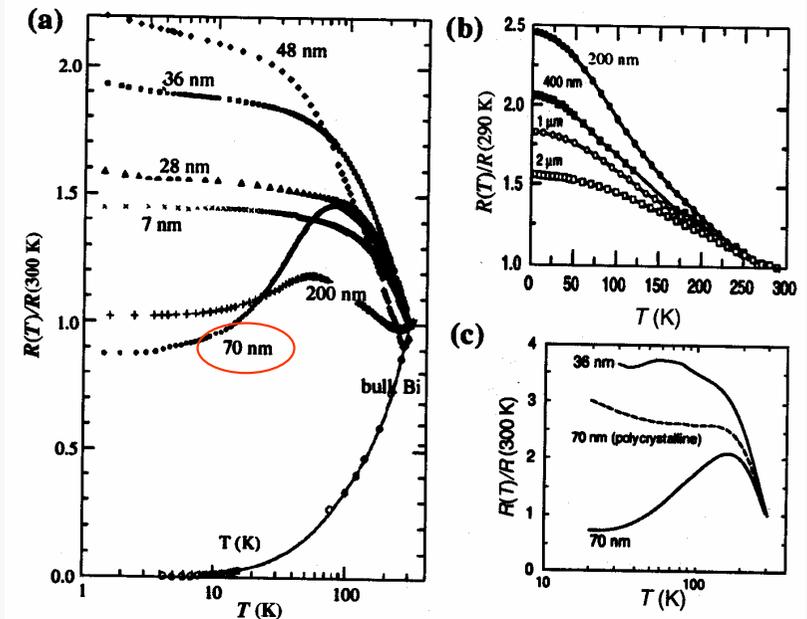

FIG. 19. (a) Measured temperature dependence of resistance for bismuth nanowire arrays of various wire diameters d_w (Heremans *et al.*, 2000). (b) $R(T)/R(290\,K)$ for bismuth wires of larger d_w measured by Hong *et al.* (1999). (c) Calculated $R(T)/R(300\,K)$ of 36-nm and 70-nm bismuth nanowires (Lin *et al.*, 2000b). The dashed curve refers to a 70-nm polycrystalline wire with increased boundary scattering.

**Extremely sensitive temp. sensors**

Mechanical properties of isolated nanostructures

Mechanical properties are affected as well by geometry and size

General trend: mechanical performances "enhanced" in nanostructures (especially stress/strain behavior, Young modulus)

Even "quantum-like" behavior of surface properties (e.g., cohesion force) can be observed (due to electronic configuration of the surface)

Measurements require suitable systems for nanoscopic investigations (e.g., Scanning Probe Microscopy, *we will see more on that!*)
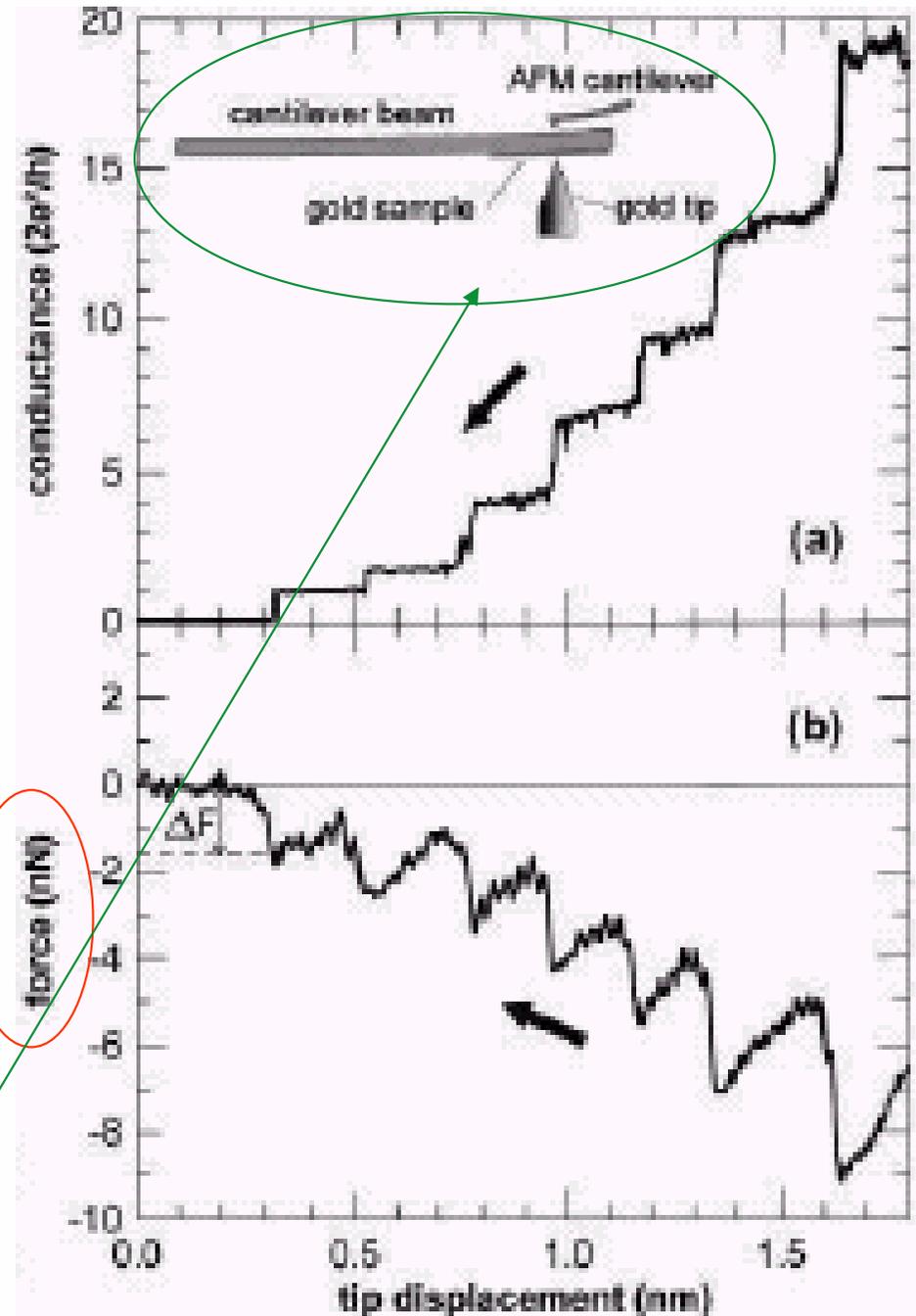
3. A very few words on nanocomposites

Practical exploitation of improved mechanical properties is usually accomplished by embedding the nanostructures in suitable matrices
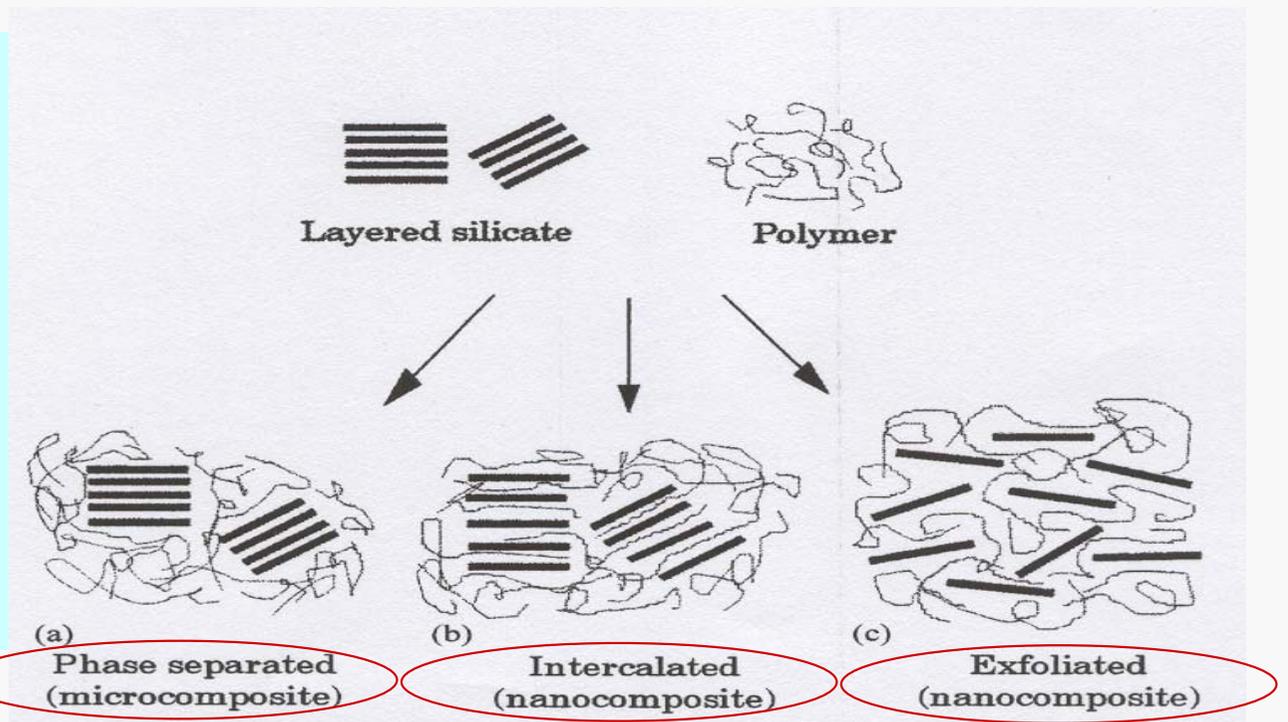
⇩

nanocomposites

Similar to already well known composite and microcomposite materials (e.g., fiberglass) but with nanosized components: phase separation should be avoided

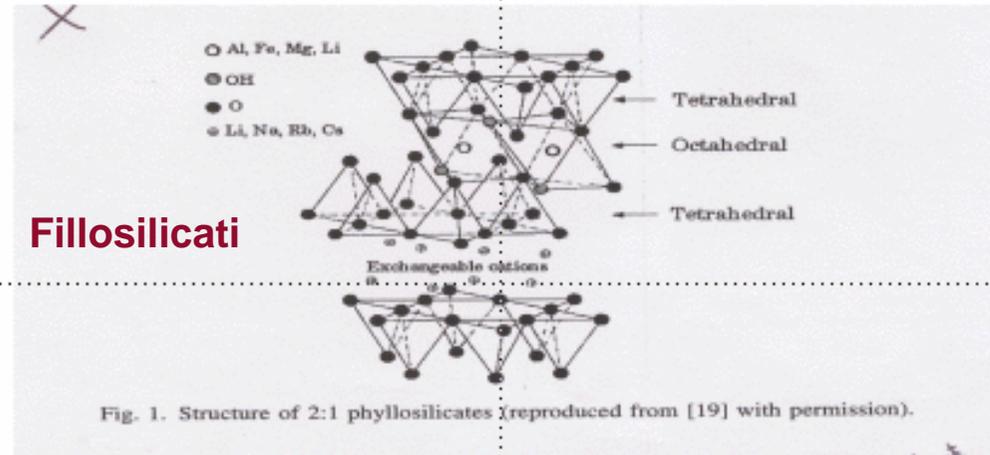Major problems: homogeneity and self aggregation of nanocomponents:

-Use of polymer matrices (**host/guest systems**)

-Dispersion in the liquid phase and special care to prevent aggregation

Layered silicate   Polymer

(a) Phase separated (microcomposite)

(b) Intercalated (nanocomposite)

(c) Exfoliated (nanocomposite)

Examples of polymer nanocomposites I

I silicati comunemente usati per i nanocompositi appartengono, come struttura, alla famiglia dei 2:1 fillosilicati

Systems made of silicates embedded (intercalated) in a polymer matrix

Fillosilicati

○ Al, Fe, Mg, Li
◉ OH
● O
◉ Li, Na, Rb, Cs

→ Tetrahedral
→ Octahedral
→ Tetrahedral

Exchangeable options

Fig. 1. Structure of 2:1 phyllosilicates (reproduced from [19] with permission).

Table 1
Example of layered host crystals susceptible to intercalation by a polymer

Chemical nature	Examples
Element	Graphite [8]
Metal chalcogenides	$(PbS)_{1.18}(TiS_2)_2$ [9], MoS_2 [10]
Carbon oxides	Graphite oxide [11,12]
Metal phosphates	$Zr(HPO_4)$ [13]
Clays and layered silicates	Montmorillonite, hectorite, saponite, fluoromica, fluorohectorite, vermiculite, kaolinite, magadiite, …
Layered double hydroxides	$M_6Al_2(OH)_{16}CO_3 \cdot nH_2O$; M=Mg [14], Zn [15]

La struttura consiste di un strato bi-dimensionale con al centro un ottaedro di alluminio o magnesio legati tramite gruppi OH a tetraedri di silicio superiori e inferiori. Ha uno spessore di circa un 1 nm e le dimensioni laterali variano da 300 Å a qualche micron.

(a)   (b)   (c)
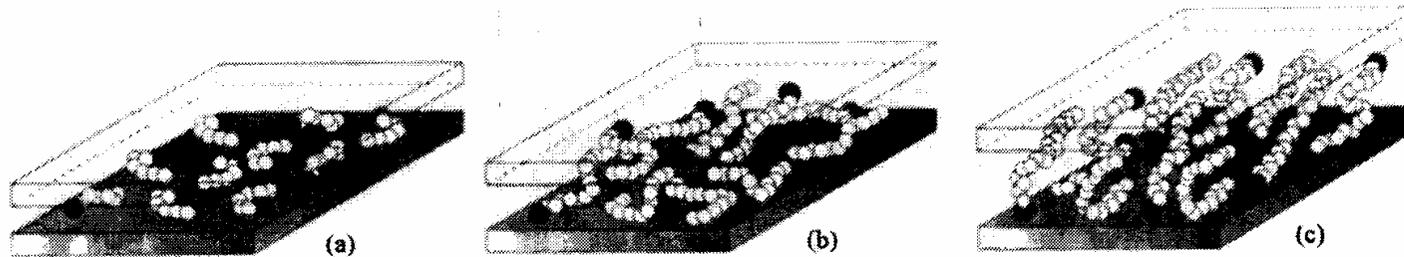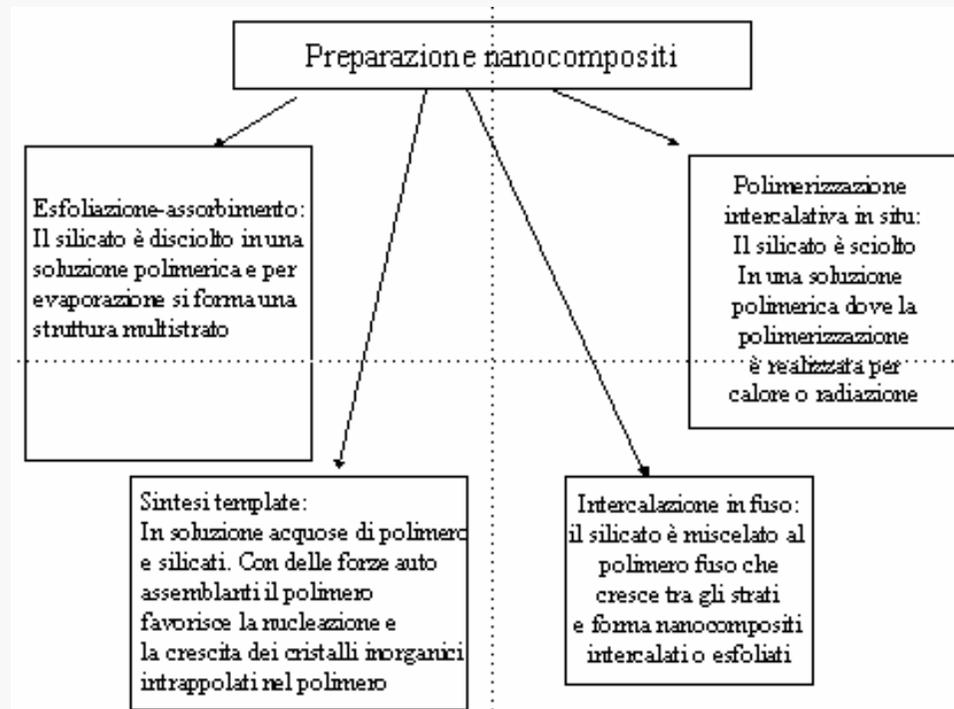
Nanostructures intercalated into a polymer matrix

Fig. 3. Alkyl chain aggregation models: (a) short alkyl chains: isolated molecules, lateral monolayer; (b) intermediate chain lengths: in-plane disorder and interdigitation to form quasi bilayers and (c) longer chain length: increased interlayer order, liquid crystalline-type environment (reproduced from [21] with permission).

Preparazione nanocompositi

Esfoliazione-assorbimento: Il silicato è disciolto in una soluzione polimerica e per evaporazione si forma una struttura multistrato

Polimerizzazione intercalativa in situ: Il silicato è sciolto In una soluzione polimerica dove la polimerizzazione è realizzata per calore o radiazione

Sintesi template: In soluzione acquose di polimero e silicati. Con delle forze auto assemblanti il polimero favorisce la nucleazione e la crescita dei cristalli inorganici intrappolati nel polimero

Intercalazione in fuso: il silicato è miscelato al polimero fuso che cresce tra gli strati e forma nanocompositi intercalati o esfoliati

Polimerizzazione intercalativa in situ

Con tale metodo sono ottenuti nanocompositi di nylon. Tra i più interessanti c'è il nanocomposito del nylon-12 tramite polimerizzazione intercalativa in situ.
Per aumentare l'adesione tra le due fasi si è usato l'acido 12-amminolaurico (ALA). In base alla quantità di ALA utilizzato si arriva ad aumentare distanza tra gli strati di silicio e a favorire l'intercalazione del polimero stesso.

Esfolazione-assorbimento

Questa tecnica è usata per polimeri idrosolubili come polivinilalcol, polietileneossido, polivinilpirrolidone o poliacidoacrilico che formano strutture esfoliate.
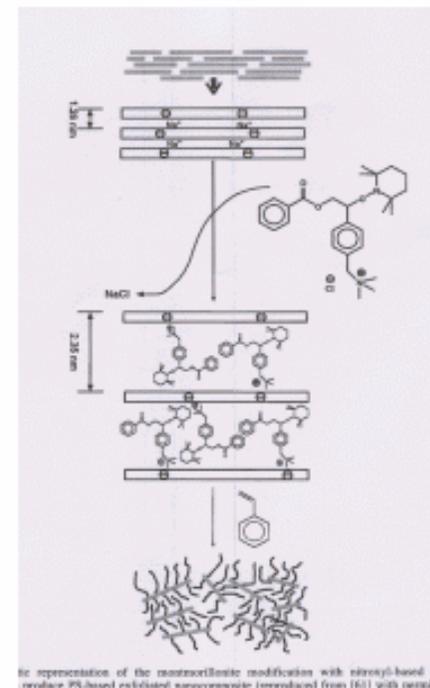
Sono stati realizzati nanocompositi con copolimeri nitrilici o con HDPE
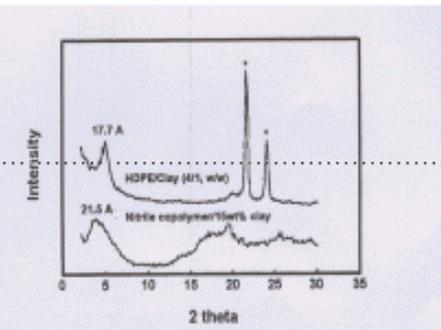
Interessanti film di nanocompositi con PLA e PCL e montmorillonite di sodio con notevoli proprietà fisiche.

Un altro interessante nanocomposto è con polistirene polimerizzato in soluzione con Na-montmorillonite in presenza di cationi organici (scambio cationico) e di iniziatori radicalici per la polimerizzazione del PS.

Per realizzare un effettiva adesione tra le due fasi e si è realizzata la polimerizzazione vivente del PS sulla superficie del fillosilicato, funzionalizzando la montmorillonite con cationi ammonio portanti gruppi nitrossidi che favoriscono la crescita del PS.

Proprietà

Gli strati di silicato hanno dimostrato un notevole miglioramento delle proprietà del polimero in cui sono dispersi. Tra queste proprietà un aumento del modulo elastico con un quantitativo circa del 1% in peso del riempitivo inorganico.
Stabilità termica, ignifughi con formazione di carbone e delle buone proprietà barriera per i gas e trasmissione di vapore.

Un notevole modulo elastico è stato mostrato anche da nanocompositi elastomerici reticolati in poliuretano che presentano una struttura esfoliata.
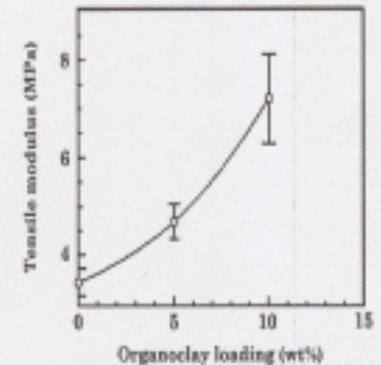
s vs. organoclay loadings for elastomeric polyurethane/clay nanocc

Proprietà meccaniche

I nanocompositi nylon-6 ottenuti per polimerizzazione intercalativa di apertura dell'anello di ε-caprolattame mostrano un notevole aumento del modulo di Young.

Altre strutture esfoliate con un un notevole modulo elastico sono i nanocompositi epossidici con ammime vulcanizzate con un 2% in peso di montmorillonite modificata con cationi alchilammonio di varia lunghezza.
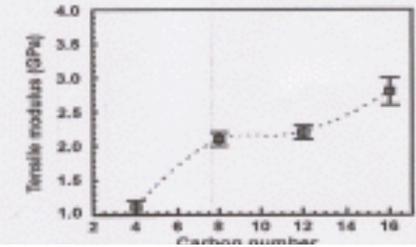
Table 12
Effect of nylon-6-based nanocomposite preparation on the Young's modulus related to the filler content and the average molecular weight of the matrix

Sample preparation	Filler content (wt.%)	MW (×10³)	Young's modulus (GPa)
Commercial nylon-6	0	13.0	1.11
NCC[a]	5	13.0	1.06
NCH[b]	4.7	16.3	1.87
L-NCH[c]	5.3	19.7	2.04
one-pot-NCH[d]	4.1	22.6	2.25

[a] NCC: montmorillonite-based nylon microcomposite.
[b] NCH: nanocomposite obtained by in situ intercalative polymerization of ε-caprolactam in protonated aminododecanoic modified montmorillonite [18].
[c] L-NCH: nanocomposite obtained by in situ intercalative polymerization of ε-caprolactam in protonated ε-caprolactam modified montmorillonite [50].
[d] One-pot-NCH: nanocomposite obtained by in situ intercalative polymerization of ε-caprolactam with Na-montmorillonite [51].

Elongazione a rottura

I nanocompositi elastomerici epossidici mostrano una significativa elongazione a rottura.
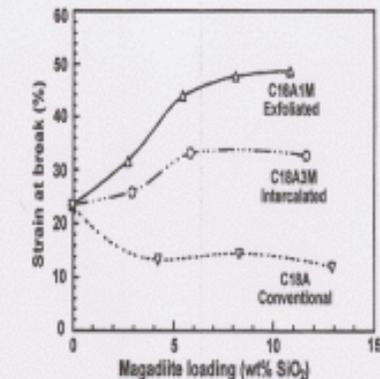Tali nanocompositi mostrano notevoli proprietà fisiche che ne fanno dei materiali ad alte prestazioni.
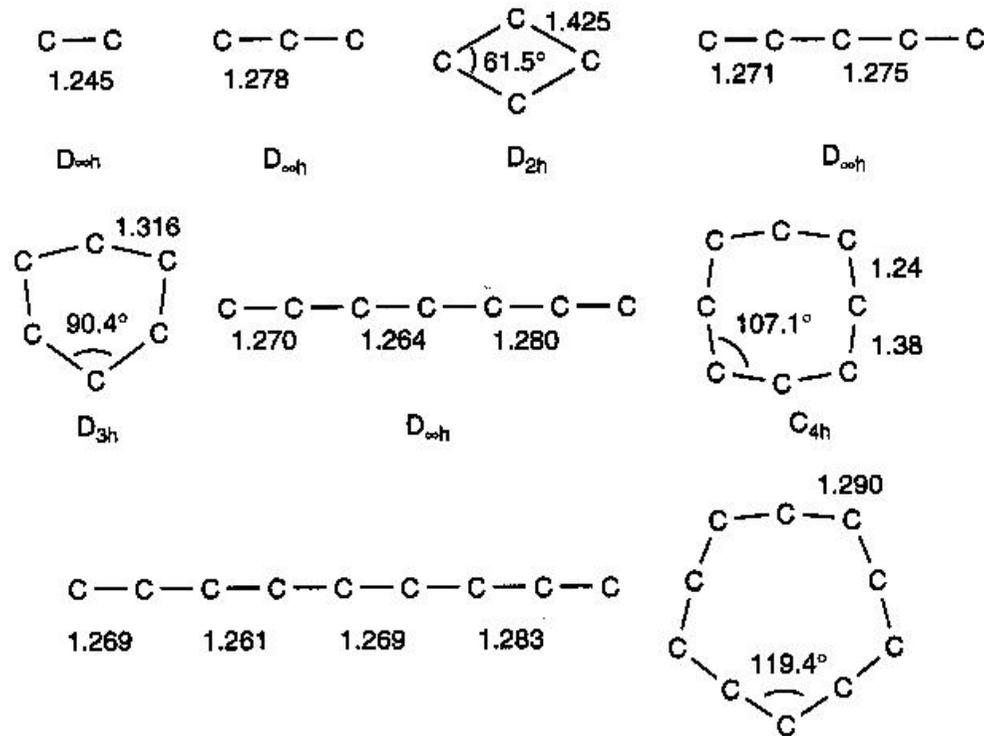
e strain at break values for an exfoliated epoxy/magadiite nano

Excellent mechanical (and chemical) properties

Key point for Carbon (*and Silicon*) chemistry: "*ibridization*"
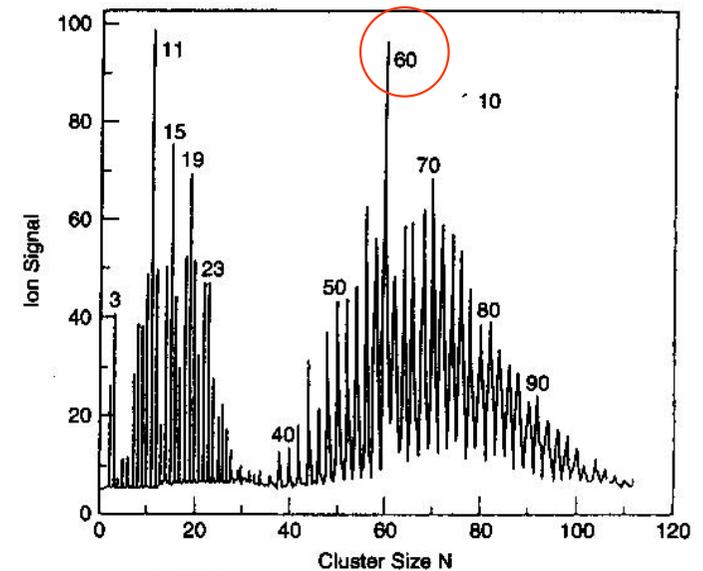Wide variety of bond angle and length between carbon atoms

Table 5.1. Types of sp^n hybridization, the resulting bond angles, and examples of molecules

Type of Hybridization	Digonal sp	Trigonal sp^2	Tetrahedral sp^3
Orbitals used for bond	s, p_x	s, p_x, p_y	s, p_x, p_y, p_z
Example	Acetylene C_2H_2	Ethylene C_2H_4	Methane CH_4
Value of λ	1	$2^{1/2}$	$3^{1/2}$
Bond angle	180°	120°	109°28′

Ion mass spectrum during pulsed laser vaporization of a graphite target

Figure 5.3. Mass spectrum of carbon clusters. The C_{60} and C_{70} fullerene peaks are evident.

Figure 5.4. Some examples of the structures of small carbon clusters. [With permission from K. Raghavacari et al., *J. Chem. Phys.* **87**, 2191 (1987).]

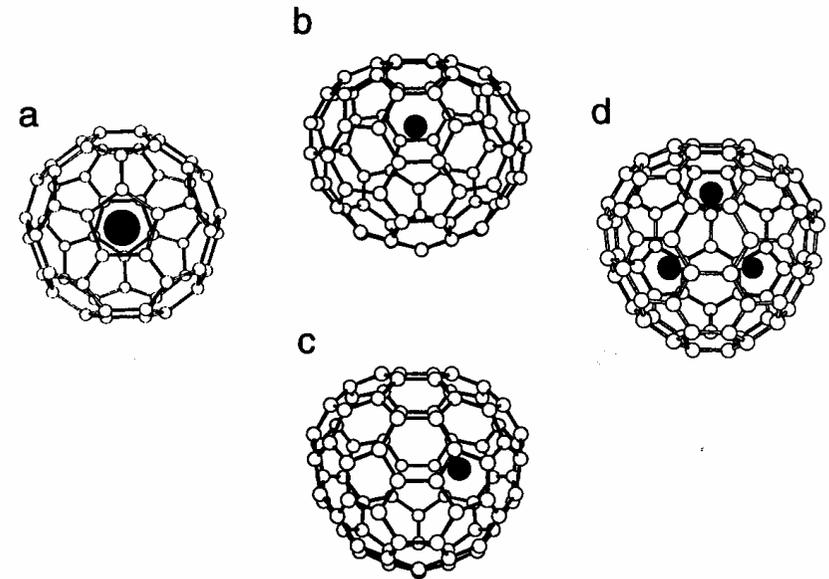**Wide variety of stable (and metastable) carbon clusters**

Fullerenes

In early gas phase work, a molecule with 60 carbon atoms was established experimentally by mass spectrographic analysis[1] as a relatively stable form relative to other carbon clusters and it was conjectured that C_{60} is a closed cage molecule with icosahedral symmetry. The name of "fullerene" was given to this family of gas phase molecules by Kroto and Smalley[1] because of their resemblance to the geodesic domes designed and built by R. Buckminster Fuller[2]. The name "buckminsterfullerene" or simply "buckyball" was given specifically to the C_{60} molecule. In the early gas phase work, the fullerene molecules were produced by the laser vaporization of carbon from a graphite target in a pulsed jet of helium[1,3].

FIGURE 2. Structural models for various endofullerenes. (a) One possible structural model for $M @ C_{60}$, with M at the center of the C_{60} cage[73]. (b, c) Two different structural models for $La @ C_{82}$, with the La at two different off-center positions within the C_{82} cage[74]. (d) A structural model for $Sc_3 @ C_{82}$ (assuming C_{3v} symmetry of the C_{82} cage), where black balls represent the three equivalent Sc^{3+} ions, which rapidly reorient within the C_{82} cage as an equilateral triangle[64].

(a) C_{60} I_h D_{5d} (b) C_{70} D_{5h} (c) C_{80} D_{5d}

(d) Armchair Nanotube D_{5h}

FIGURE 1. Examples of closed shell fullerene configurations which avoid dangling bonds: (a) C_{60}, (b) C_{70}, (c) C_{80} and (d) an armchair carbon nanotube. Also indicated on the figure are the point group symmetries of the various structures. We note that D_{5d} is a subgroup of the icosahedral group I_h, exhibiting inversion symmetry.

The cage-like structures can be filled (endohedrically doped) with metal atom(s) leading to peculiar electronic properties (e.g., superconductivity)

Magic nunbers exist (e.g., 60, 72, 80, etc) for stable C_n clusters with specific cage-like structures
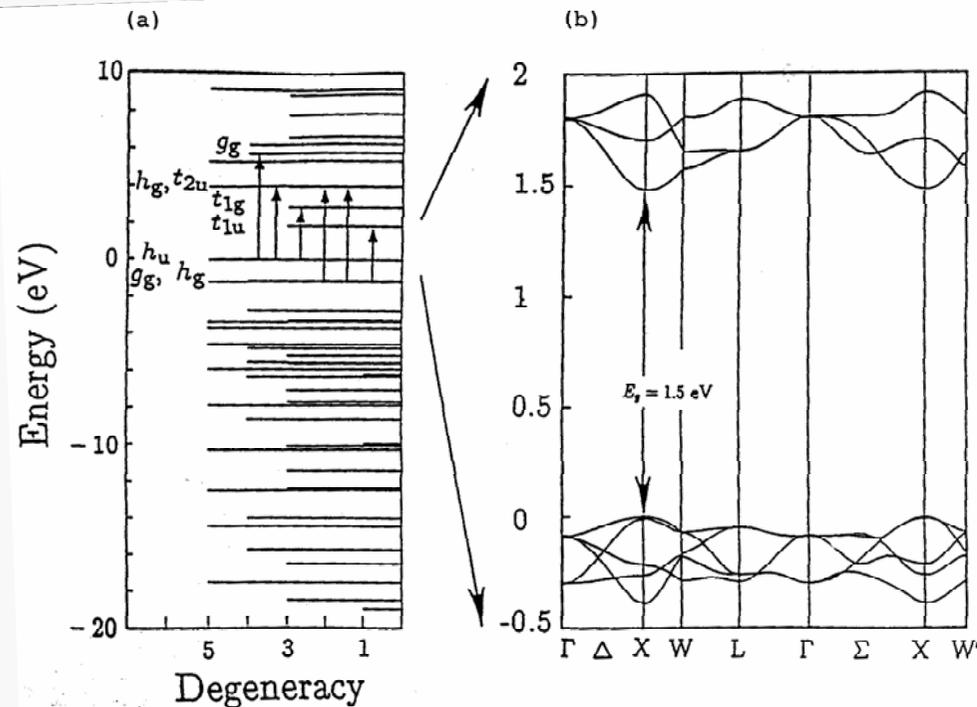
Fullerite

FIGURE 7. Calculated electronic structure of (a) an isolated C_{60} molecule and (b) FCC solid C_{60} where the direct band gap at the X-point is 1.5 eV[106].

Deposition and growth of fullerene-based films results in a FCC structure (**fullerite**) with typical semiconducting properties

TABLE 1. Physical constants for C_{60} molecules and for crystalline C_{60}

Quantity	Value	Reference
Average $C-C$ distance	0.144 nm	[19]
$C-C$ bond length on a pentagon	0.146 nm	[5,20]
$C-C$ bond length on a hexagon	0.140 nm	[5,20]
C_{60} mean molecule diameter	0.710 nm	[18]
Moment of inertia I	1.0×10^{-43} kg m^2	[21]
Volume per C_{60}	1.87×10^{-22}/cm^3	–
Number of distinct C sites	1	–
Number of distinct $C-C$ bonds	2	–
Binding energy per atom[a]	7.40 eV	[22]
Heat of formation (per g C atom)	10.16 kcal	[23]
Electron affinity	2.65 ± 0.05 eV	[24]
Cohesive energy per C atom	1.4 eV/atom	[25]
Spin-orbit splitting of $C(2p)$	0.00022 eV	[26]
Ionization potential	7.58 eV	[27]
Optical gap[b]	1.9 eV	[22]
fcc lattice constant	1.417 nm	[28]
$C_{60}-C_{60}$ distance	1.002 nm	[17]
$C_{60}-C_{60}$ cohesive energy	1.6 eV	[29]
Mass density	1.72 g/cm^3	[17]
Molecular density	1.44×10^{21}/cm^3	[17]
Transition temperature (T_{01})	261K	[34]
Vol. coeff. of thermal expansion	$6.1 \times 10^{-5} K^{-1}$	[37]
Band gap (HOMO-LUMO)	1.7 eV	[38]
Work function	4.7 ± 0.1 eV	[39]
Thermal conductivity (300K)	0.4 W/mK	[43]
Electrical conductivity (300K)	1.7×10^{-7} S/cm	[44]
Static dielectric constant	$4.0 - 4.5$	[45,46]
Melting temperature	1180°C	[47]
Sublimation temperature	434°C	[48]
Heat of sublimation	40.1 kcal/mol	[48]
Latent heat	1.65 eV/C_{60}	[49]

[a] The binding energy for C_{60} is believed to be ~0.7 eV/C atom less than for graphite although literature values for both are given as 7.4 eV/C atom. The reason for the apparent inconsistency is attributed to differences in calculational techniques.
[b] Calculated value for the optical band gap for the free C_{60} molecule.

Carbon NanoTubes (CNT)

The earliest observations of carbon tubules with very small (nanometer) diameters[110,113,114] were based on high resolution transmission electron microscopy (TEM) measurements, providing evidence for μm-long tubules, with cross-sections showing several concentric coaxial tubes and a hollow core. In Figure 8, the first published observations of carbon nanotubes are shown[110]. Here we see only multi-layer carbon nanotubes, but one tubule has only two coaxial carbon cylinders [Figure 8(b)], and another has an inner diameter of only 2.3 nm [Figure 8(c)][110]. These carbon nanotubes were prepared by a carbon arc process (typical dc current of 50–100 A and voltage of 20–25 V) where carbon nanotubes in the form of tubule bundles are found on the negative electrode, as the positive electrode is consumed in the arc discharge[116]. Typical lengths of the arc-grown tubules are ~1 μm, giving rise to an aspect ratio (length to diameter ratio) of 10^2 to 10^3. Because of their small diameter, involving only a small number of carbon atoms, and because of their large aspect ratio, carbon nanotubes are classified as 1D carbon systems. Most of the theoretical work on carbon nanotubes emphasizes their 1D properties. In the multilayered carbon nanotubes, the measured (by high resolution TEM) interlayer distance is 0.34 nm[110], in good agreement with the value of 0.339 nm for the average equilibrium interlayer separation, obtained from self-consistent electronic structure calculations[117,118].

Although very small diameter (less than 10 nm) carbon filaments, were observed many years earlier on vapor grown carbon fibers[119,120], no detailed systematic studies of such very thin filaments were reported in the 1970's and 80's. A direct stimulus to the systematic study of carbon filaments of very small diameters came from the discovery of fullerenes by Kroto, Smalley, and coworkers[1], and subsequent developments resulting in the synthesis of gram quantities of fullerenes by Krätschmer, Huffman and coworkers[8]. These recent developments heralded the entry of many scientists into the field, together with many ideas for new carbon materials and bringing
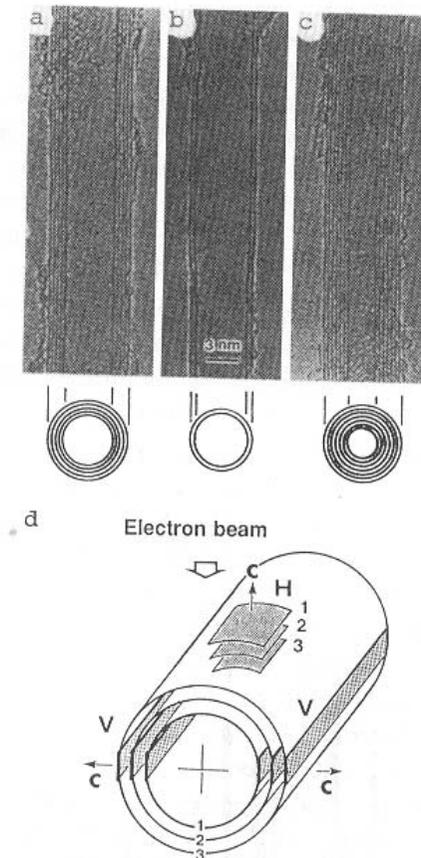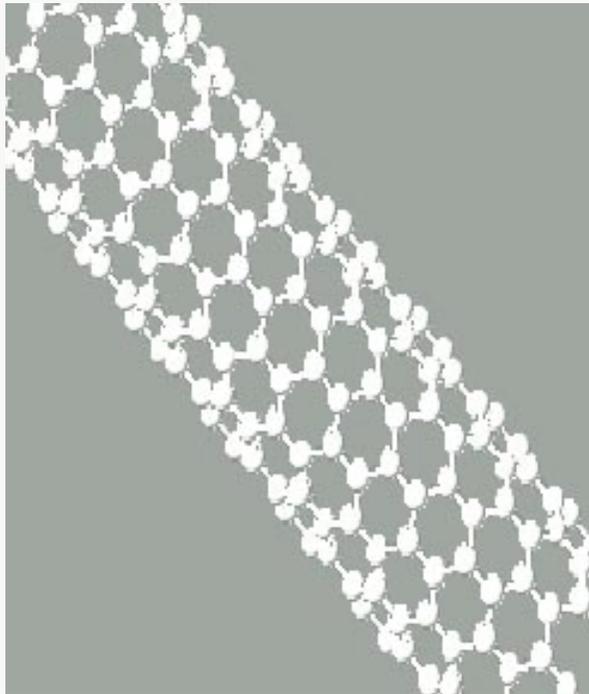

FIGURE 8. The observation of N concentric carbon tubules with various inner diameters d_i and outer diameters d_o reported by Iijima using TEM. (a) $N = 5$, $d_o = 6.7$ nm, (b) $N = 2$, $d_o = 5.5$ nm, and (c) $N = 7$, $d_i = 2.3$ nm, $d_o = 6.5$ nm. Each cylinder is described by its diameter and chiral angle. The sketch (d) indicates how the interference pattern for the parallel planes labeled H are used to determine the chiral angle θ, which is the angle between the tubule axis and the nearest zigzag axis defined in Figure 10[110].

Work on fullerenes produced a revival of interest for (already known) *filamentary carbon nanostructures (nanotubes)*
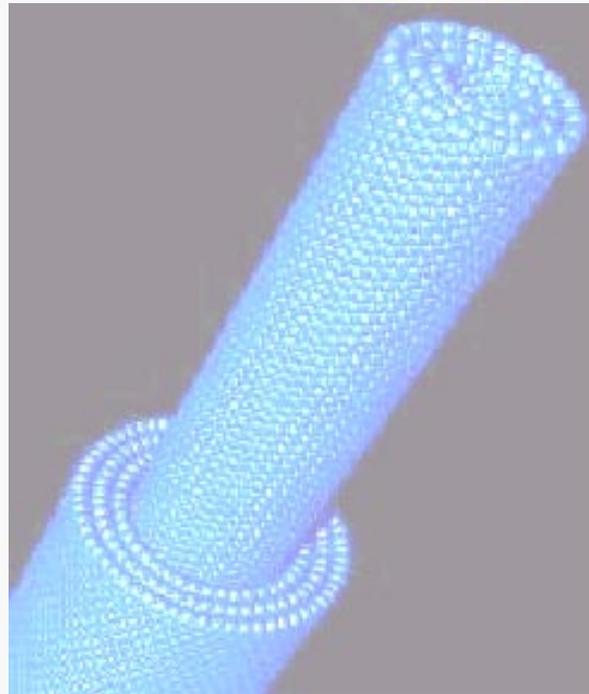
Single and multiwall CNT

CNT: a graphite plane (graphene) is wounded in a cylindrical shape

SWNT: single nanotube
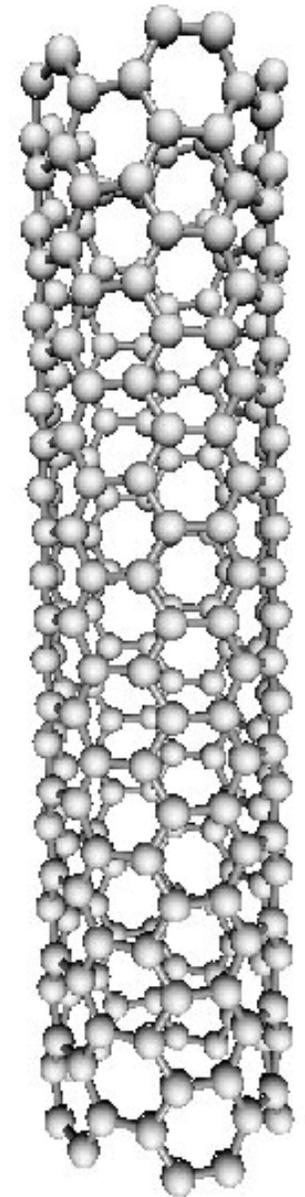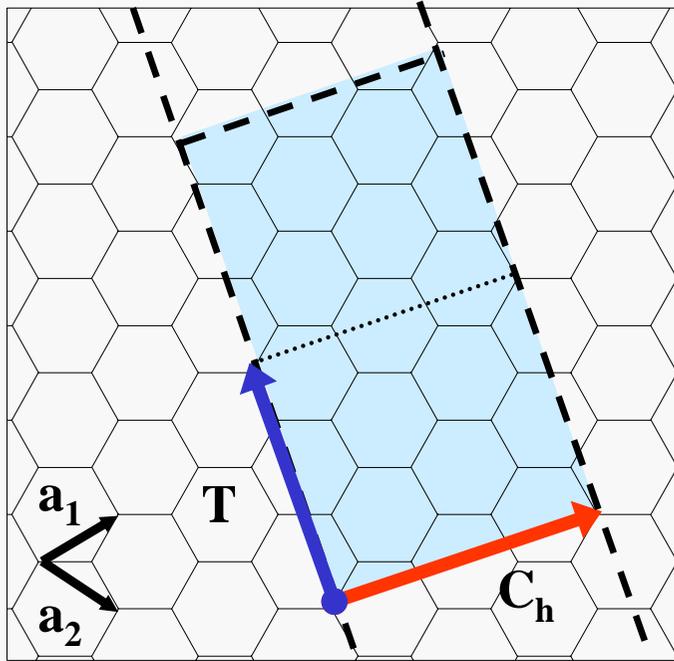**MWNT: concentric nanotubes with different diameters**

Single Wall NT

Multiple Wall NT

Materiale sui CNT tratto in parte da un seminario di Andrea Ferrari,
EDM - Cambridge University (lug. 2002)
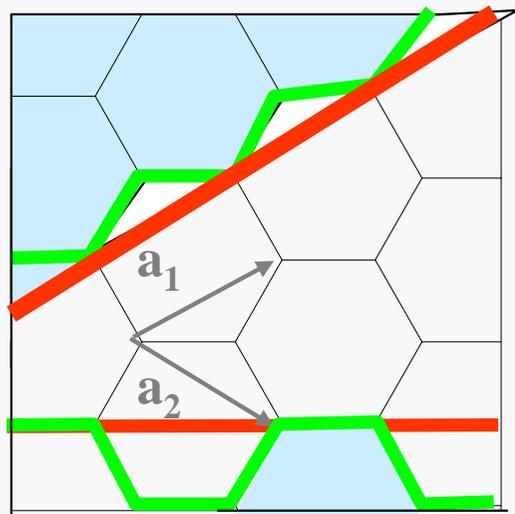
CNT families

1D structures with sp^2 bonds

Unit cell described by:

- chiral vector

  $$\mathbf{C_h} = n\mathbf{a_1} + m\mathbf{a_2} \equiv (n, m) \; \forall \; n,m \in Z$$

- translation vector

  $$\mathbf{T} = t_1\mathbf{a_1} + t_2\mathbf{a_2} \;\; \forall \; t_1, t_2 \in Z$$

Zigzag (n, 0) tube
$\mathbf{C_h} \parallel \mathbf{a_1}$ (or $\mathbf{a_2}$)

Armchair (n, n) tube

[Chiral (n, m) tube]

CNT diameter: $d_{NT} \propto \sqrt{(m^2 + n^2 + nm)}$

CNT structure uniquely determined by (n, m)

First neighbor distance ~ 1.42 Å
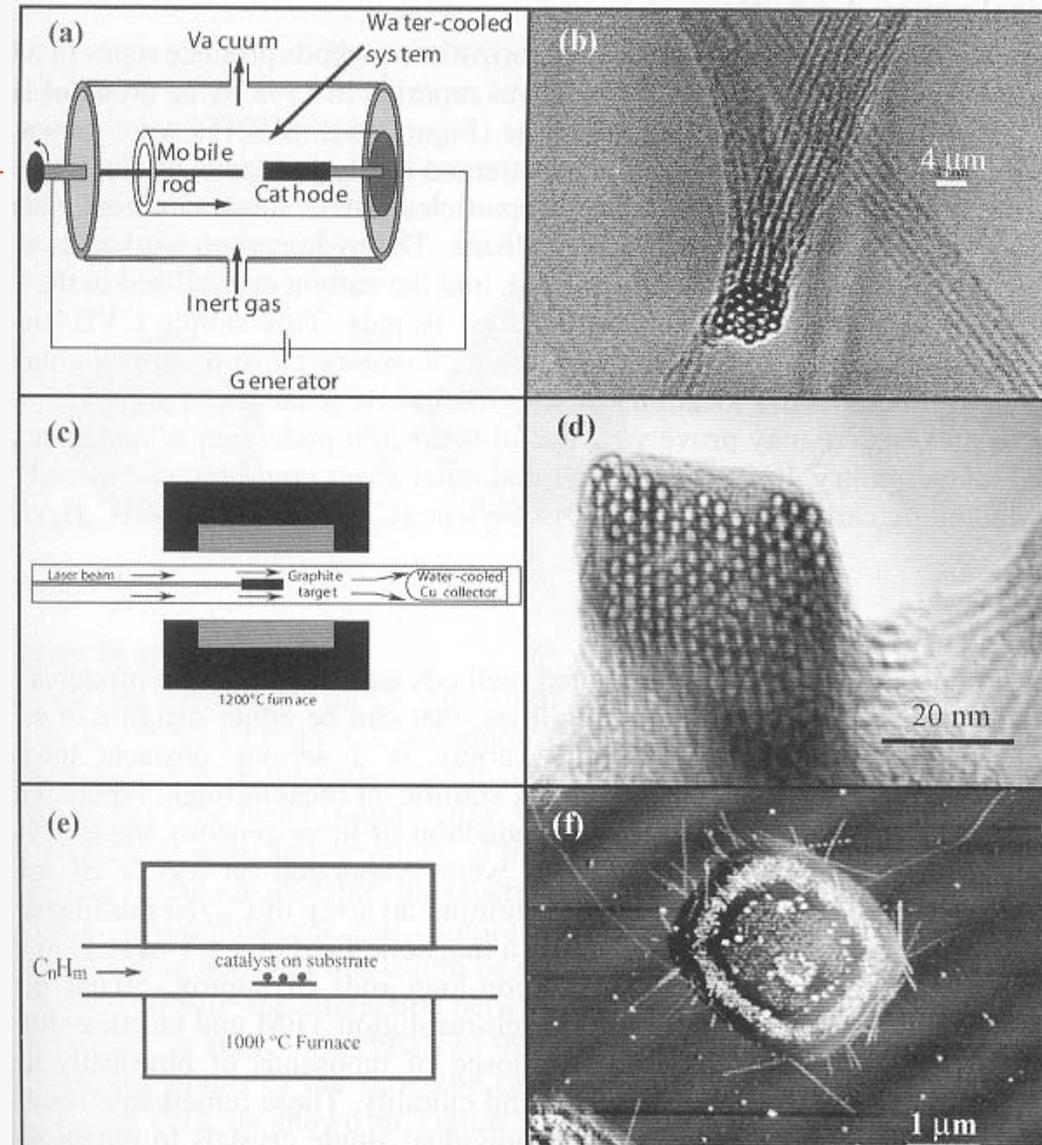
CNT fabrication I

Nanotubes can be produced by many techniques
Typically vapour phase is involved to produce nanotubes from carbon atoms
Typically "violent" methods are required to induce strong collisional situation

Electric arc discharge (similar to fullerene)

Laser ablation (similar to clusters)

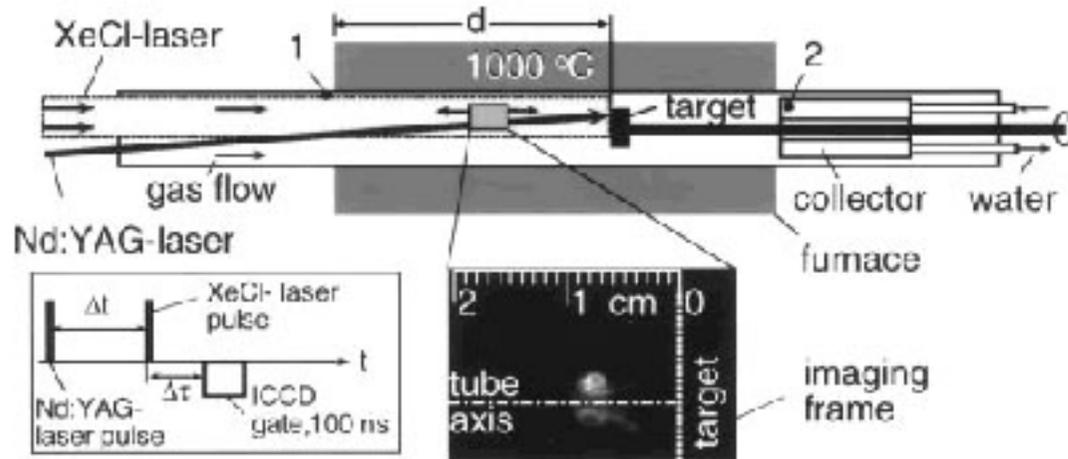**Plasma Ehnanced Chem Vap Dep (PE-CVD)**

Chemical Vapor Deposition

CNT fabrication II

Pulsed Laser Ablation --> SWCNT with good diameter control
Arc discharge --> large rates, low control (mostly MWCNT)
PE-CVD from C_xH_x --> large rates, fair control

Laser Ablation

Fig. 1. Schematic of the 2″-diameter quartz tube and hot furnace used for laser vaporization growth of SWNT with in situ LIL-imaging and spectroscopy diagnostics. Beam geometries and imageable area are indicated. The *black dots* and the *numbers* show the collection points of the ablated material: 1-upstream; 2-collector. The C/Ni/Co target was positioned at two distances, *d*, from the front of the furnace. The *inset on the left* shows the relative timing between ablation (Nd:YAG) and and LIL-probe (XeCl) laser pulses (Δt), and the ICCD gate delay after the XeCl laser, ($\Delta \tau$)

PE-CVD
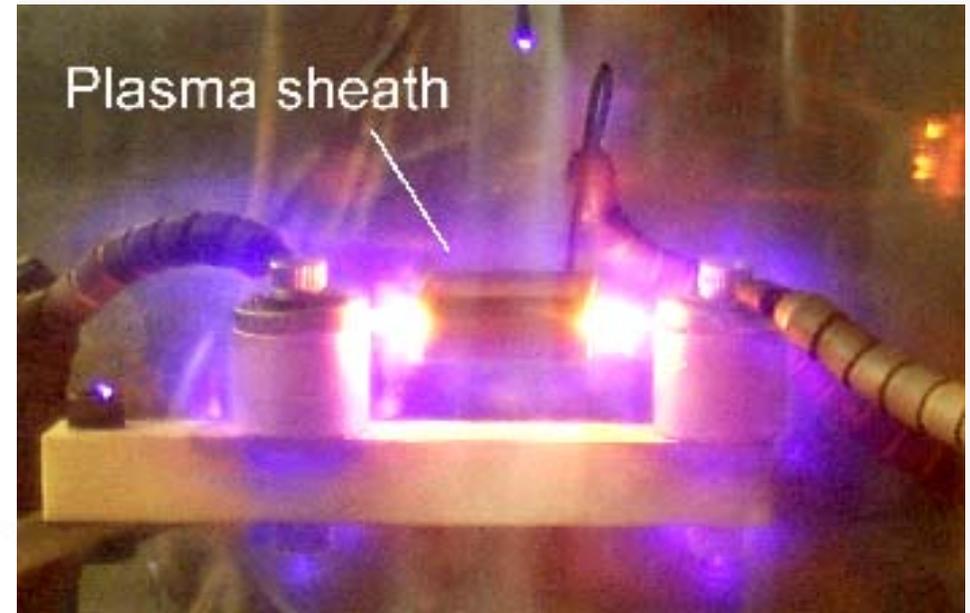

- Up to 900°C heated stage
- C_2H_2/NH_3 up to 200sccm

See Puretzky, Geohegan,…
Appl. Phys. A <u>70</u> 153 (2000)

Role of catalyzers I

Root-growth mechanism

The root-growth mechanism for the growth of an individual SWNT from a metal nano-particle on a substrate by the CVD method is schematically represented in Figure 16. First the hydrocarbon decomposes on the metal nanoparticle into hydrogen and carbon, which dissolves in the metal (Figure 16a). When the carbon becomes super-saturated in the nanoparticle, it starts to precipitate in the form of a graphitic sheet. Since the edges of the graphitic sheet are unstable, the emergence of *pentagon defects*, leading to the formation of a curved fullerene cap (Figure 16b), becomes energetically favored, as it allows the dangling bonds of this cap to be stabilized by coordination with the metal. As in the catalytic models, the interaction between the partially filled 3d orbitals of the transition metal and the empty π^* orbitals of the carbon, may play a crucial role in stabilizing the dangling bonds of the fullerene cap. After the cap is formed, two things can happen. In one case, as shown in Figure 16a, more carbon atoms can insert into the metal-carbon bonds, leading to the elongation of the fullerene, and the growth of a SWNT. Otherwise (not shown), the fullerene cap can keep growing around the nanoparticle, eventually engulfing it, and preventing any further growth. The competition between these two pathways should determine the yield of SWNT growth. An analogous mechanism has been proposed for the growth of SWNT ropes from larger metal nanoparticles from carbon vapors, produced either by arc discharge or laser vaporization.

Metal nanoparticles (typ Ni or Co) used to enhance nanotube formation
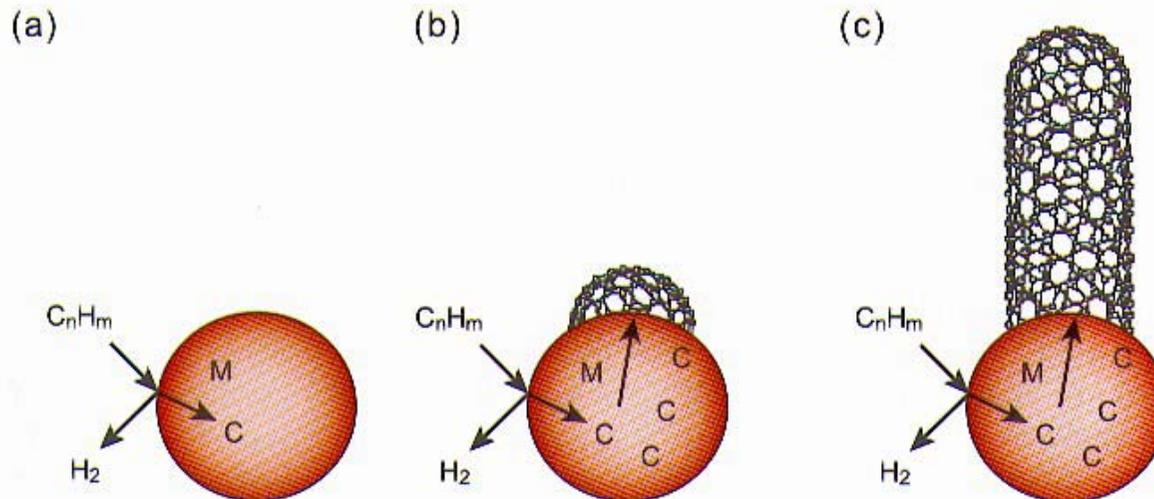
Figure 16: Root-growth mechanism for the formation of a single-wall carbon nanotube from a metal nanoparticle, by chemical vapor deposition:
(a) decomposition of the hydrocarbon on the nanoparticle and solubilization of the carbon therein.
(b) nucleation by formation of a fullerene cap.
(c) elongation of the SWNT by incorporation of further carbon into the metal-carbon bonds at the growing end.

Role of catalyzers II
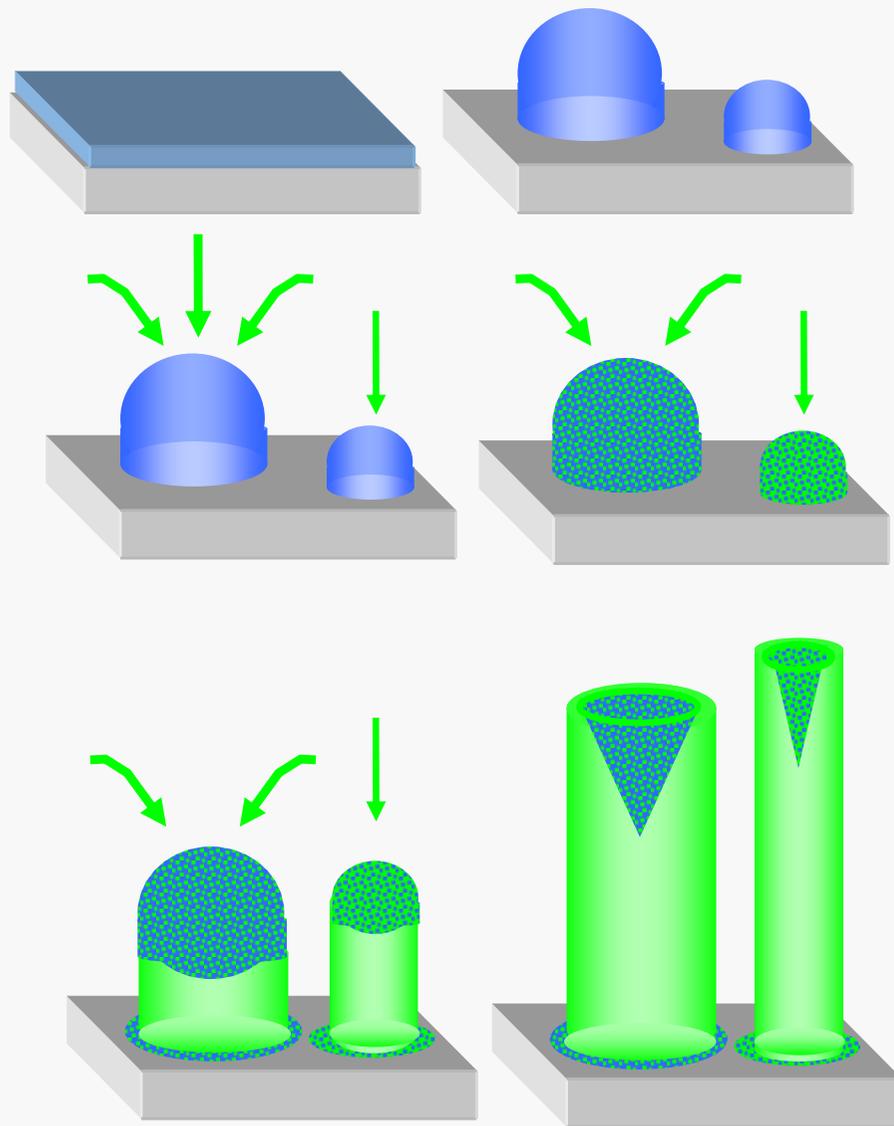
**Alternative picture
(Vapor Liquid Solid –
VLS method)**

- During annealing/etching the metal layer dewets the substrate forming droplets
- Carbon dissolves into the catalyst material and forms a solid solution
- After saturation, carbon precipitates starting the NT growth
- The metal droplet is lifted at the growing edge

Role of catalyzers III

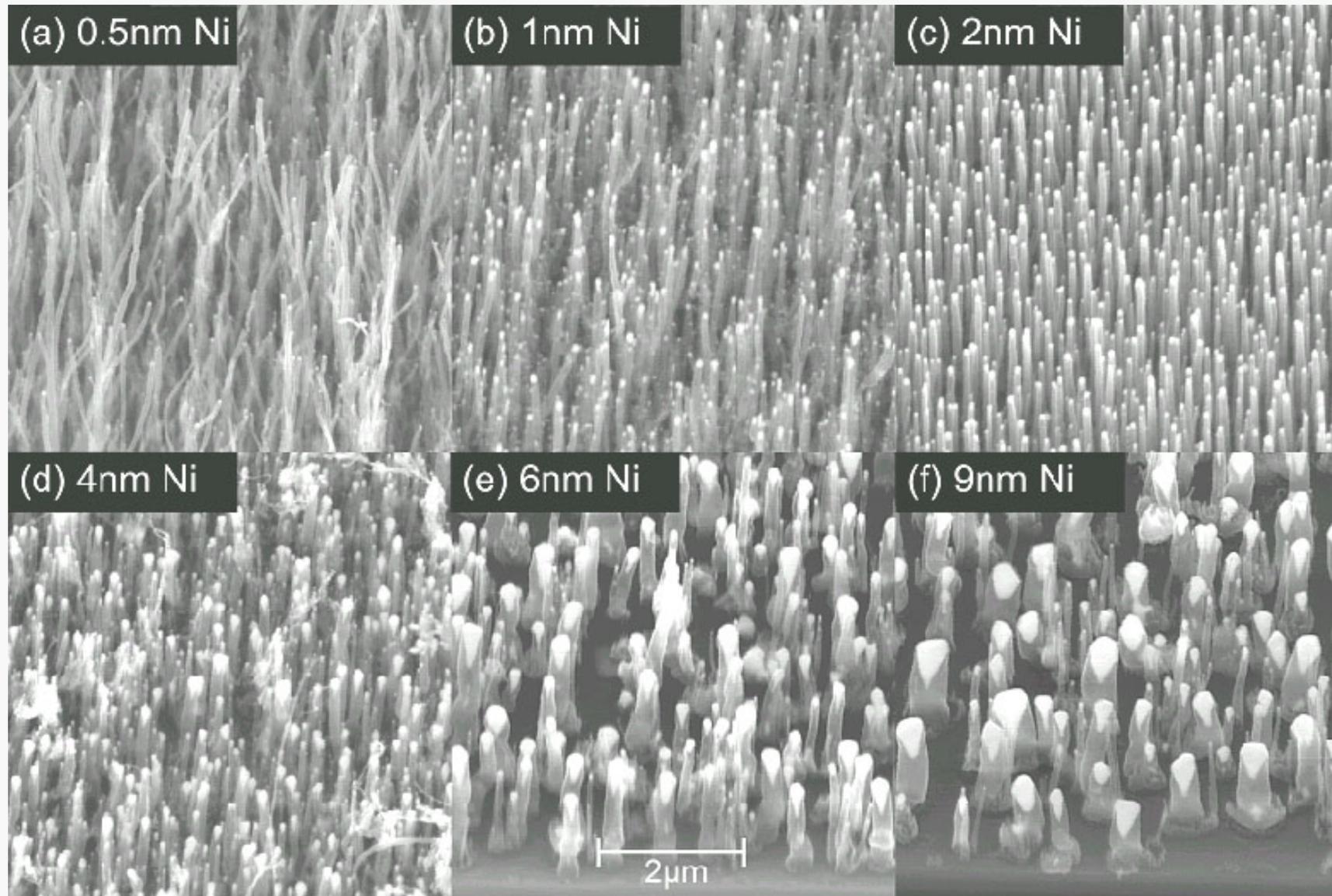Metal nanoparticles can be "deposited" onto the substrate

⇩

If a nanoparticle pattern is structured onto the substrate,
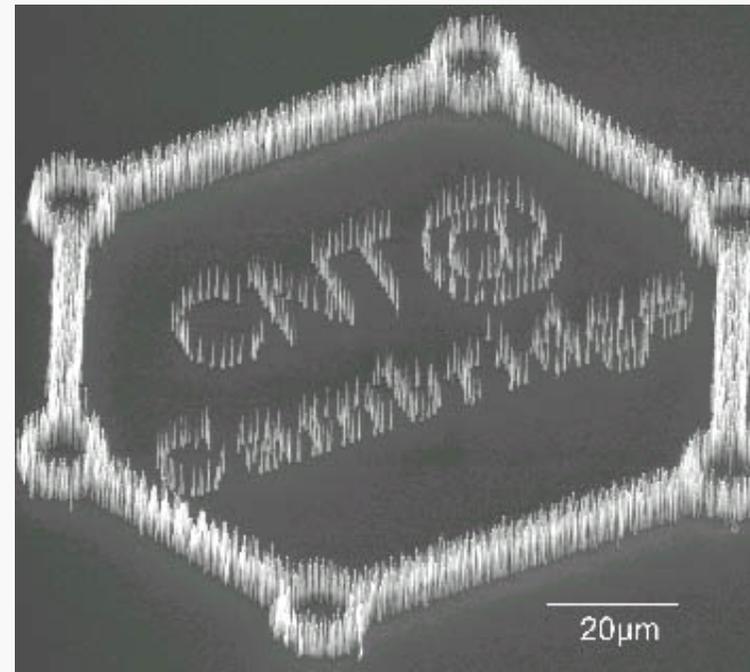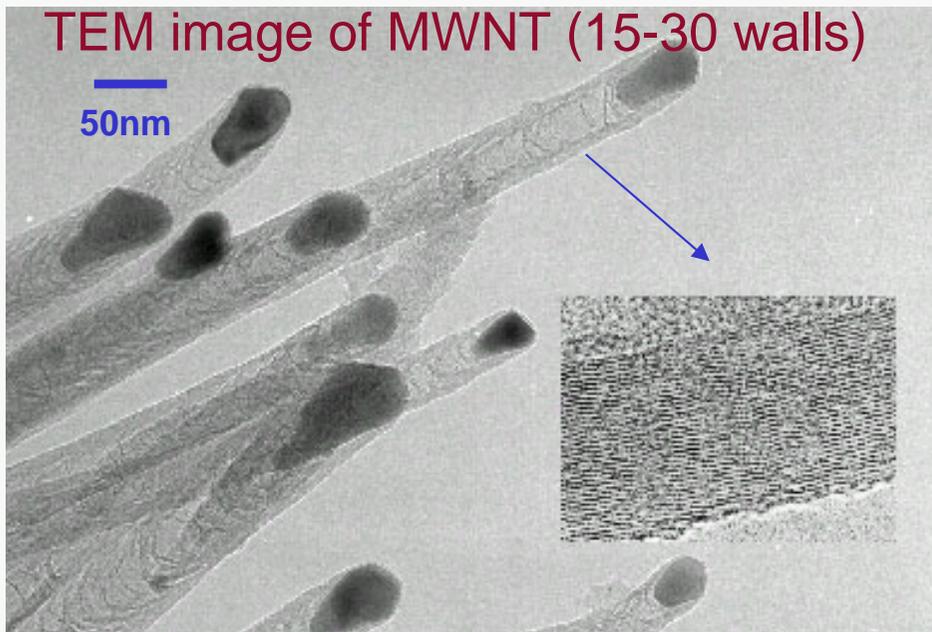structured CNT growth can be achieved
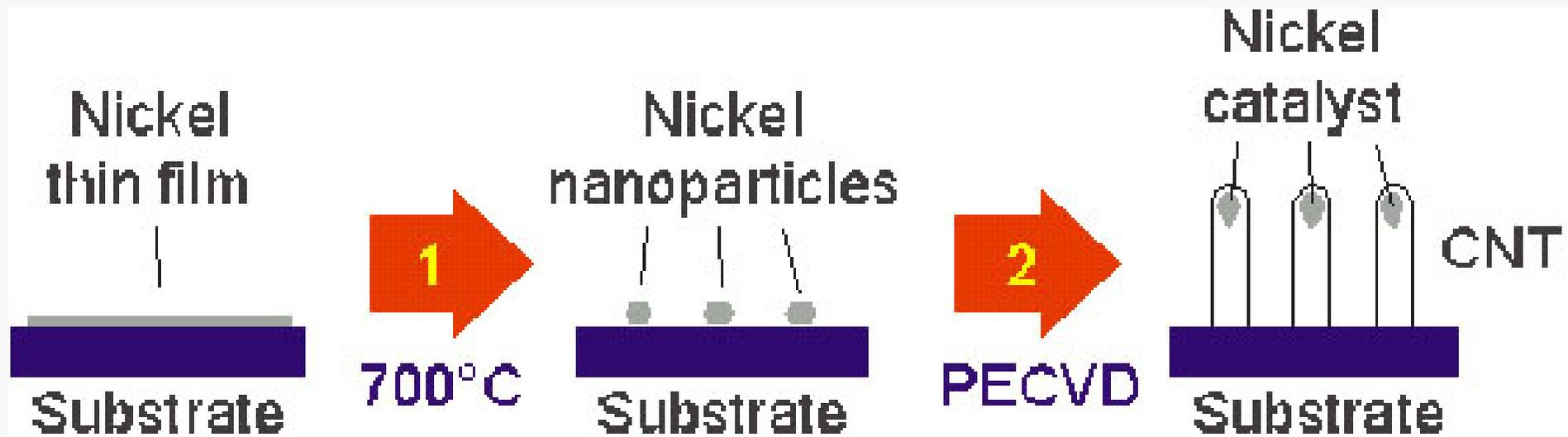
- **Step 1**: At 700°C (growth temp), Ni film sinters into catalyst nanoparticles.
- **Step 2**: PECVD - C_2H_2 is the growth gas for CNTs, NH_3 is the etching gas for unwanted a-C.

Role of catalyzers IV

Effect of nanoparticle size in CNT growth

(a) 0.5nm Ni (b) 1nm Ni (c) 2nm Ni (d) 4nm Ni (e) 6nm Ni (f) 9nm Ni 2µm

CNT patterns

TEM image of MWNT (15-30 walls)

50nm

20μm

Nanoparticle patterns can be achieved by lithography leading to CNT patterns

Figure 18: Nanotube blocks created by catalyst mediated growth. The tubes are generated from iron catalyst pads (100 × 100 μm) patterned by the lift-off technique. The first inset shows that each block consists of numerous nanotubes with a length exceeding 100 μm. The second inset shows a TEM-image of a single nanotube revealing that the tubes are multi-wall with about 16 shells and a diameter of approximately 20 nm.

1μm

5 nm

1μm

EHT = 5.00 kV   Signal A = In Lens
WD = 5 mm   Photo No = 978
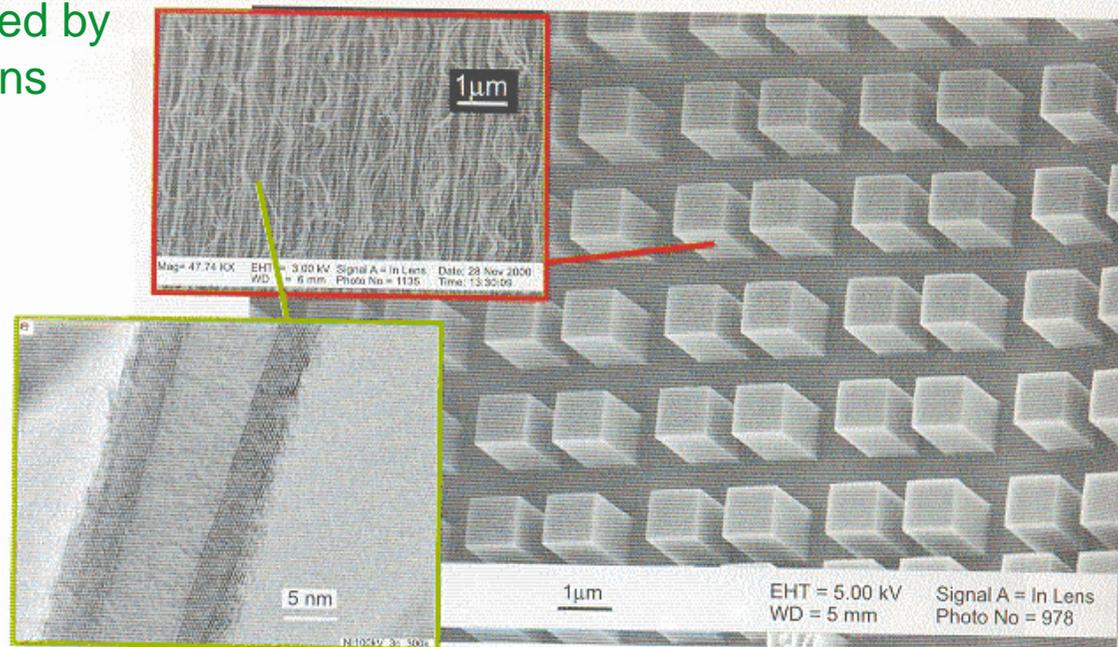
# Envisioned applications of CNT

Applications other than electronics:

- Hydrogen and ion (Li) storage units
- Supercapacitors, fuel cells, batteries
- Gas sensors
- FE devices **(field emitters)**
- Advanced scanning probes (SEM)
- Superstrong and tough composites **(nanocomposites)**
- Templates for metal nanowires
- Actuators **(NanoElectroMechanical Systems - NEMS)**
- ...

Many applications exploit the unique mechanical properties and the 1D geometry
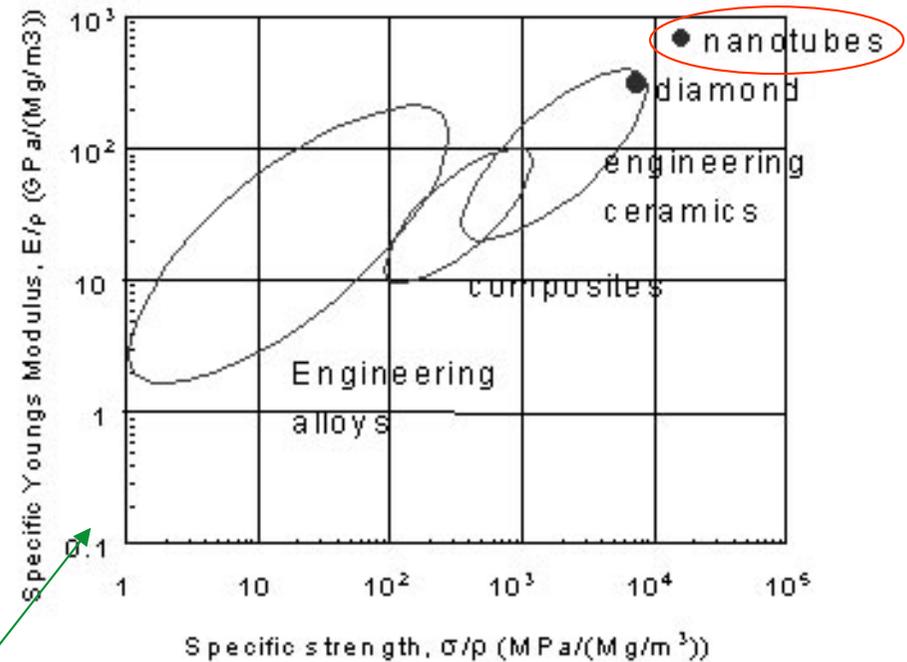
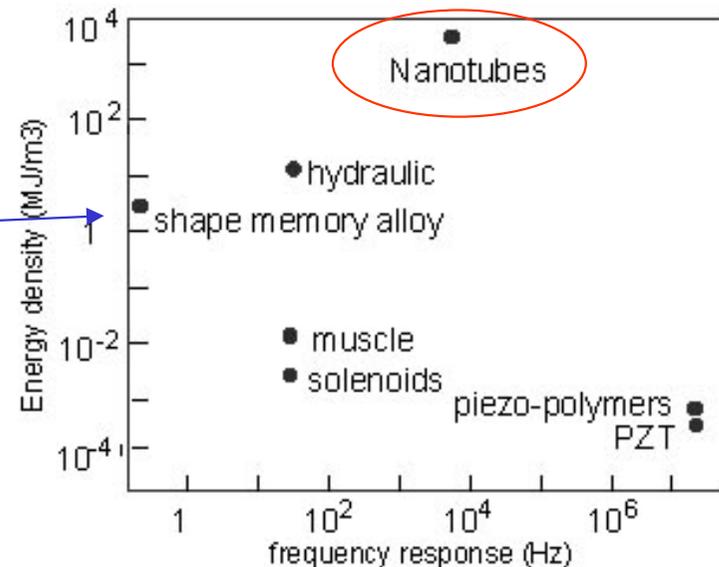Comparison of Specific Young's Modulus vs. Specific Strength for nanotubes and other engineering materials

Fig. 3. Energy Density vs. Frequency response of Actuator materials

5. Mechanical properties of CNT composites

Tensile strength (GPa)

Carbon Nanotubes | Graphite Fibres | Aramid (Kevlar) | Stainless Steel
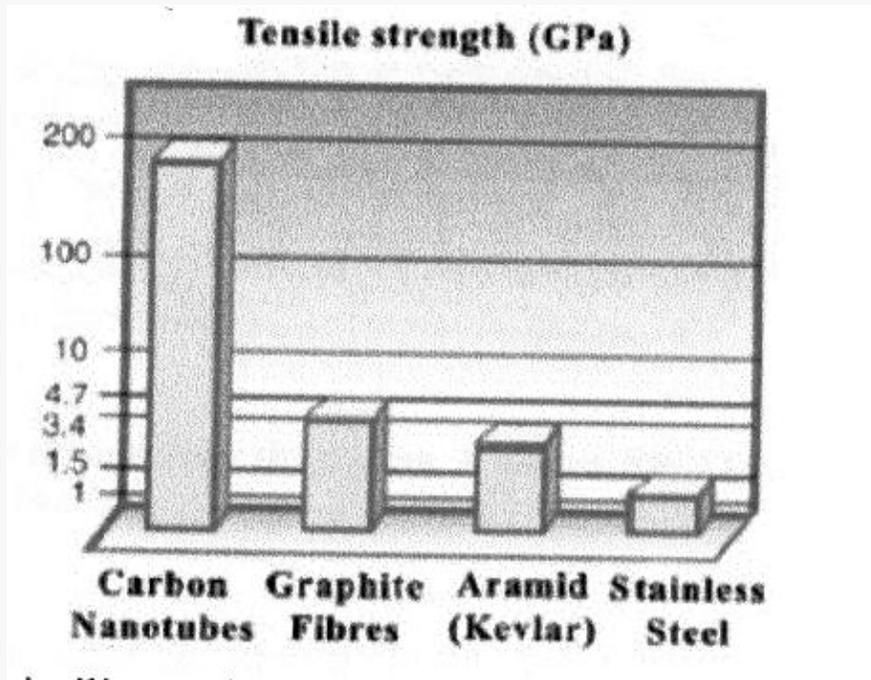
Young, shear and bulk modulus similar to diamond

Excellent mechanical properties due to strong intercarbon bonds and cylindrical geometry

⇩

Exploitations in structural materials
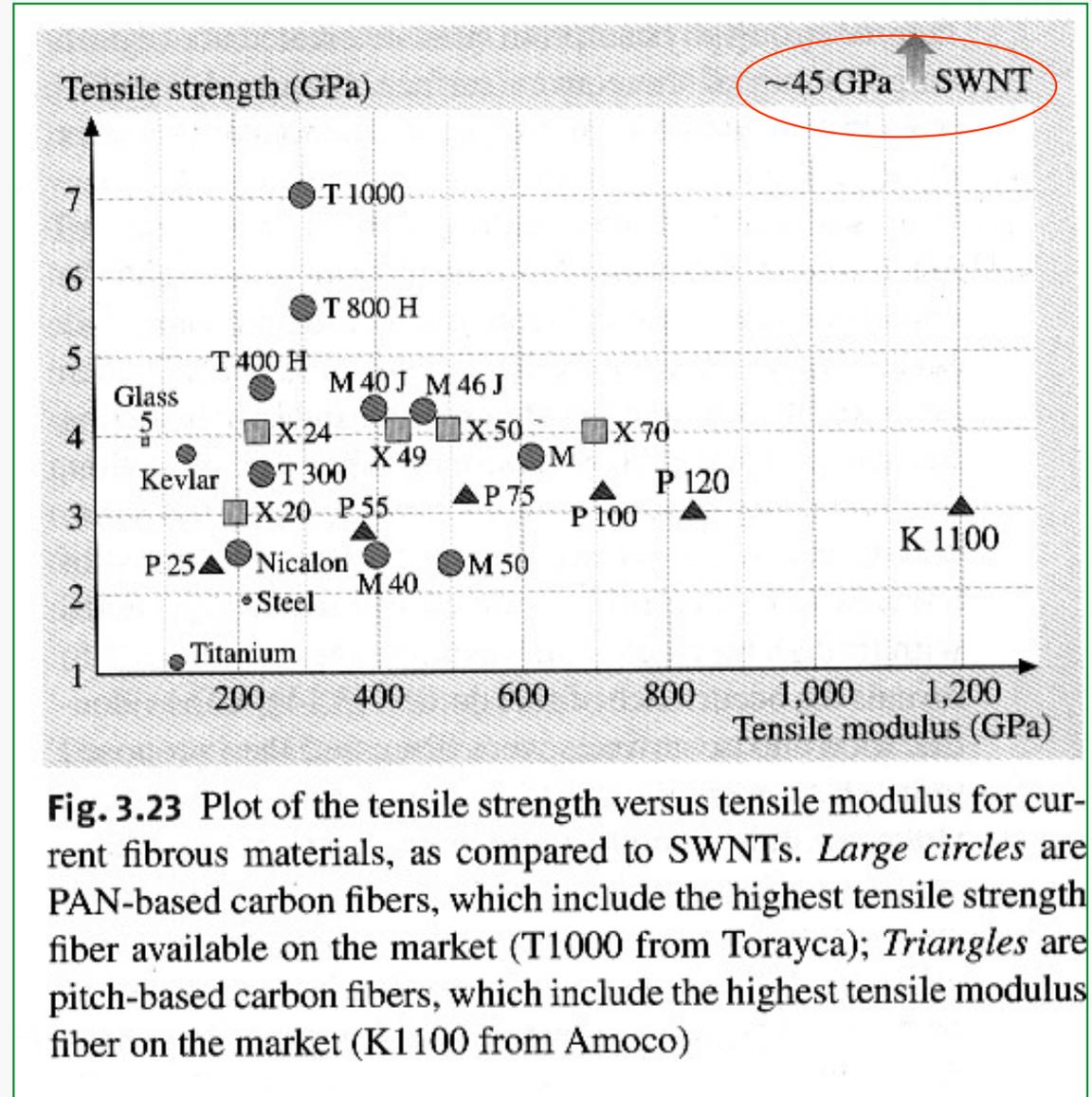
Fig. 3.23 Plot of the tensile strength versus tensile modulus for current fibrous materials, as compared to SWNTs. *Large circles* are PAN-based carbon fibers, which include the highest tensile strength fiber available on the market (T1000 from Torayca); *Triangles* are pitch-based carbon fibers, which include the highest tensile modulus fiber on the market (K1100 from Amoco)

Ductility/brittleness problems in CNT
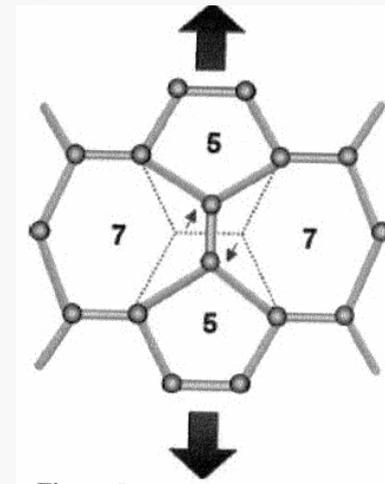
Stone Wales deformation

Figura 23 – (a) Mappa dei domini duttile/fragile per nanotubi di carbonio con diametri fino a 13 nm. Aree con diversa ombreggiatura corrispondono a differenti comportamenti del materiale; (b) Processo di 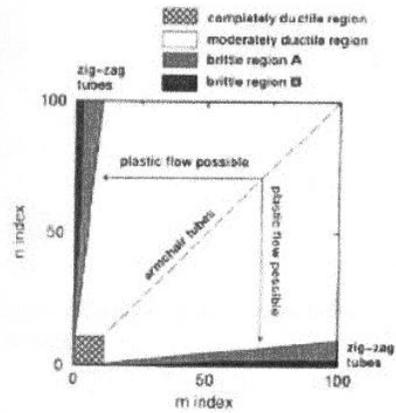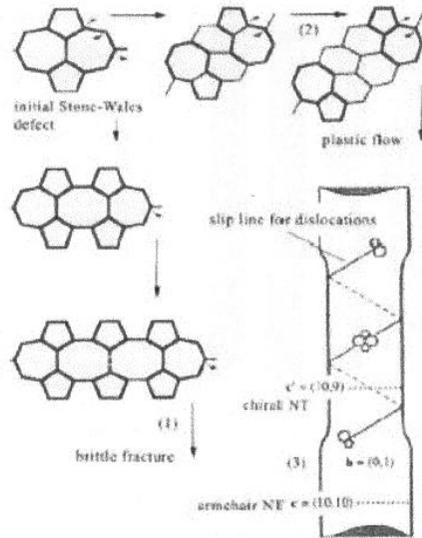propagazione di difetti in un nanotubo armchair con un iniziale difetto Stone-Wales. (1) frattura; (2) una coppia di dislocazioni scivolano via l'una dall'altra; (3) il cambio di chiralità del nanotubo e il graduale cambiamento del diametro causano una corrispondente variazione nelle proprietà elettriche. La formazione di ulteriori difetti Stone-Wales continua il processo di restringimento a meno che le dislocazioni non si impilino a causa della bassa temperatura che limita la mobilità sui tubi.
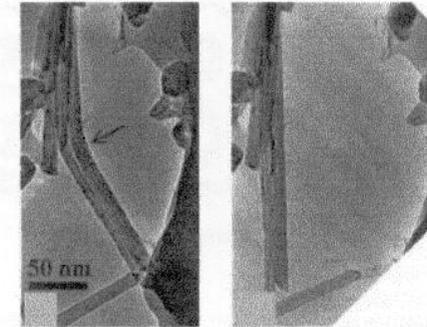
Figura 27 – Due immagini TEM mostrano un nanotubo (sx) originariamente piegato a temperatura ambiente e (dx.) dopo il riscaldamento

Heating up can restore the deformation
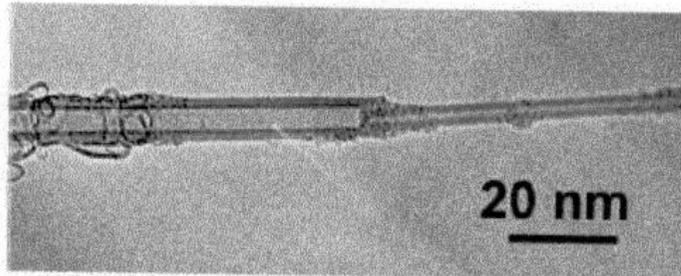
Figura 21 - Immagine TEM. Il nucleo interno a 4 strati è stato estratto (comportamento telescopico).

Telescopic behavior of MWNT under traction forces

Nanoscopic investigations of the mechanical properties

Fig. 25.1 Schematic showing the details of a nanoscale bending test. The AFM tip is brought to the center of the nanobeam and the piezo is extended over a known distance. By measuring the tip displacement, a load-displacement curve of the nanobeam can be obtained [25.38]

D_{tip} = sensitivity × dV_{AFM}

$D_{beam} = D_{piezo} - D_{tip}$

$F_{beam} = F_{tip}$ = stiffness of cantilever × D_{tip}

AFM can be used to apply local (and controlled) deformations

Stress/strain (and fracture) by AFM
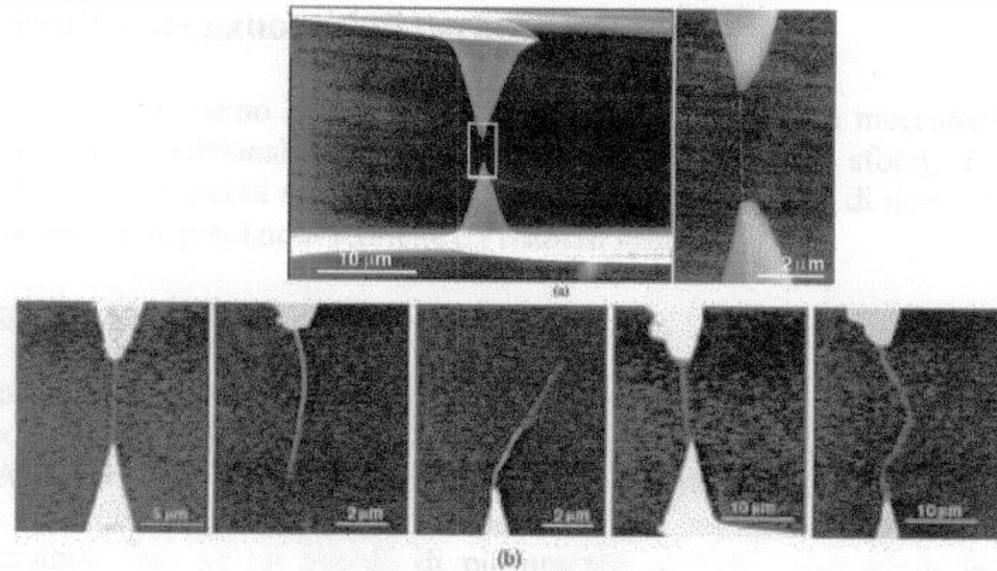
- Immagini SEM che mostrano (a) l'apparato per la misura di carico tensile di MWCNT con un taccato a due punte AFM opposte prima dell'imposizione del carico; (b) il meccanismo di frattura "telescopico" tipico dei MWCNTs.
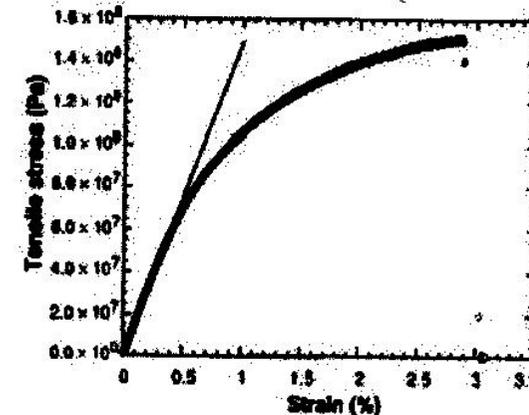
Figura 20 - Grafico stress-strain in misure tensili condotte su fibre di SWCNT.

Multifunctional CNT nanocomposites

Table 3.5 Applications for nanotube-based multifunctional materials (from [3.3]), by courtesy of B. Maruyama (WPAFB, Dayton, Ohio)

Fiber fraction	Applications system	Mechanical			Electrical			Thermal		Thermo-mechanical	
		Strength/stiffness	Specific strength	through-thickness strength	Static dissipation	Surface Conduction[a]	EMI shielding	Service temp.[b]	conduction/dissipation[c]	Dimensional Stability[d]	CTE reduction[e]
Low Volume fraction (fillers)											
Elastomers	Tires	×			×					×	
Thermo	Chip package				×					×	
Plastics	Electronics/Housing	×				×	×			×	
Thermosets	Epoxy products	×	×	×	×					×	×
	Composites			×						×	
High Volume Fraction											
Structural composites	Space/aircraft components		×	×							
High conduction composites	Radiators	×						×	×		
	Heat exchangers	×						×	×		×
	EMI shield	×					×				

[a] For electrostatic painting, to mitigate lightning strikes on aircraft, etc.
[b] To increase service temperature rating of product
[c] To reduce operating temperatures of electronic packages
[d] Reduces warping
[e] Reduces microcracking damage in composites

Wide variety of applications for CNT nanocomposites

Embedding CNT in polymer matrix

CNT/polivinylalcohol

Compatibility is an issue to avoid separation of CNT with respect to the matrix

Examples of functionalization

shortened-*SWNT*—CH$_2$CH$_2$(OCH$_2$CH$_2$)$_n$OCH$_3$

n = 41 ⇒ PEG 2000

R$_1$-NH-CH$_2$-CO$_2$H + R$_2$CHO → [...] →

DMF, riflusso, 120 h
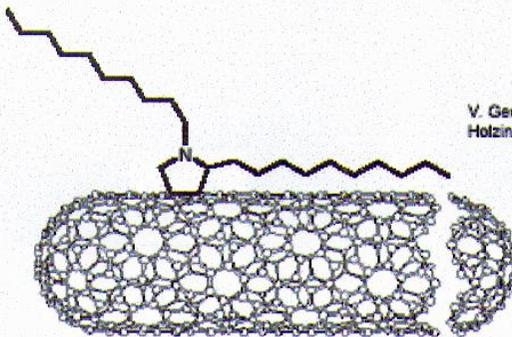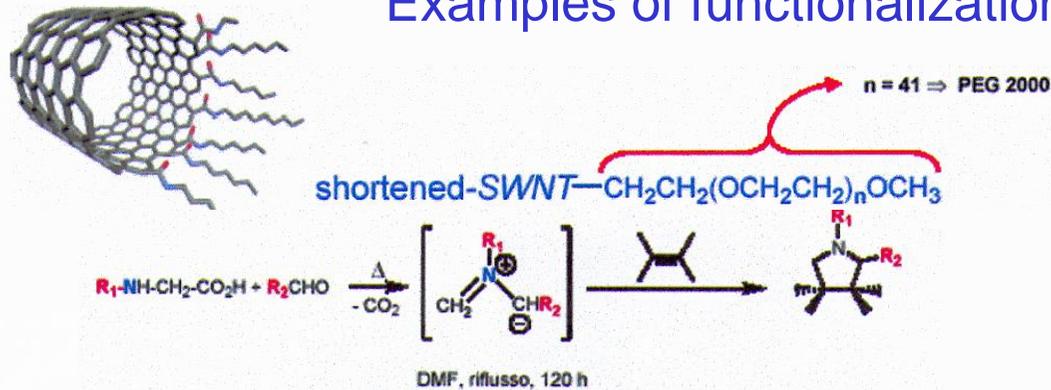
V. Georgakilas, K. Kordatos, M. Prato, D. M. Guldi, M. Holzinger, A. Hirsch, J. Am. Chem. Soc. **2002**, 124, 760-761.

Figura 26 – Immagine SEM della superficie si frattura in un composito a base di nanotubi di carbonio.

CNT funzionalizzato per solubilizzarlo in matrici polimeriche (es.: polietilenglicole attaccato a estremità di CNT "spezzati", oppure AIBN - azobisiso butirronitrile che inizia legami covalenti tra carbonio e PMMA)

oppure surfattanti non-ionici per aumentare wettability

oppure miscelamenti meccanici prolungati (Brabender a doppia vite e temperatura alta)

Figura 32 – (sx) Immagine TEM di un composito MWNT (4% in peso) in una matrice di PMMA. La freccia bianca indica la direzione del taglio (90° rispetto alla direzione di estrusione). Le frecce nere indicano i nanotubi. (dx) Istogramma che riporta la distribuzione di orientazione di MWCNT nel composito. La linea tratteggiata corrisponde a un fitting Lorentziano dei dati.

Other examples of CNT functionalization

Una prima reazione prevede la sospensione dei nanotubi in una solu-
zione 3:1 di acido solforico e nitrico in un bagno sonico per due ore,
quindi per reazione con PDADMAC (polidiallildimetilammonio-
Cloruro) che si aggancia ai gruppi carbossilici presenti in superficie,
le particelle d'oro con diametro di 10 nm possono aderire:

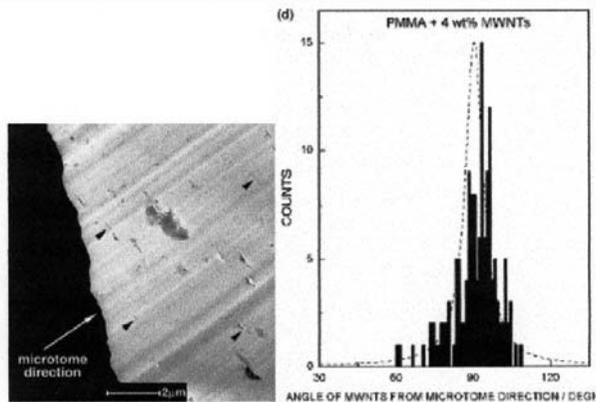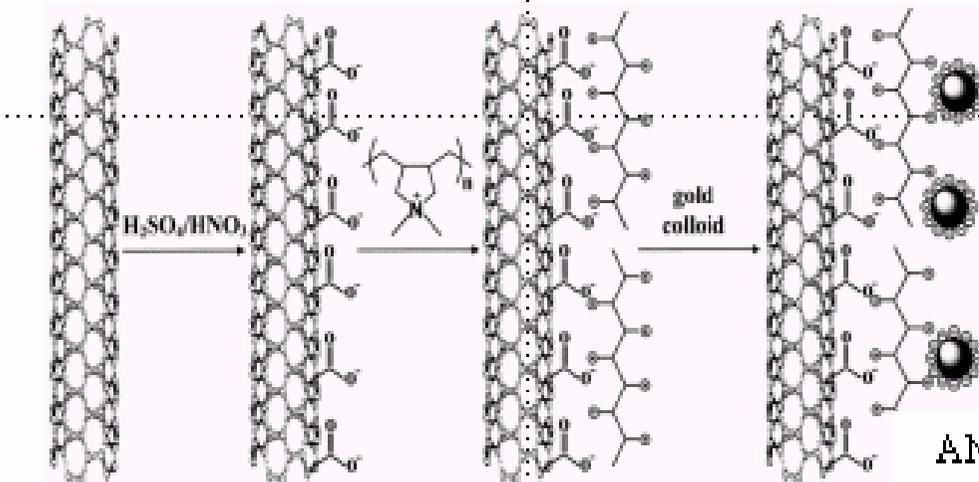
Schematizzazione dell'attacco dei cluster di oro sulla superficie
dei nanotubi:
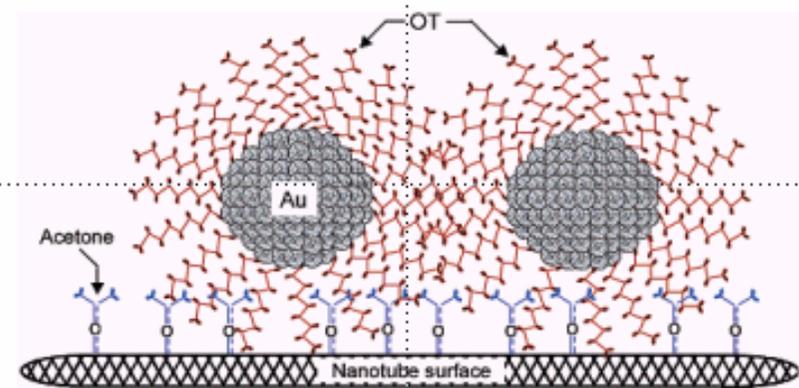
ANCORAGGIO DI NANOCLUSTER D'ORO SULLA SUPERFICIE
DI NANOTUBI DI CARBONIO MODIFICATI

Gold nanoparticles can be "attacked" to CNT
wall through:
-Stabilization of nanoparticles by thiol (or
ammine) groups
-An adhesion agent is interposed between
CNT wall and the nanoparticle

Further developments expected to lead to
CNT functionalization by proteins or other
biocompatibles

La modifica con acetone della superficie dei nanotubi di carbonio permette
l'adesione di cluster metallici.
Nanoparticelle d'oro stabilizzate da opportuni leganti come tioli (o ammine)
possono essere dunque adese su tali superfici dando luogo a strutture che potranno
essere impiegate in nanodispositivi ibridi bio-inspired.
Infatti c'è un grande studio sulla possibilità di far aderire opportuni cluster
stabilizzati da proteine su questi nanotubi quali parte di nanodispositivi.
Per quanto riguarda il meccanismo di attacco esso è stato ipotizzato dai valori degli
stretching asimmetrici dei CH_2 e CH_3 prima e dopo l'attacco dei cluster sui nanotubi
e la conclusione è che si tratti di un'interazione tra le catene alchiliche dell'OT
(ottandiolo) con i gruppi metilici dell'acetone.

Materiale tratto dal seminario di
M. Barnabò, Aprile 2004

6. Electronic properties of CNT: from graphite to CNT

Highly Oriented Pyrolithic Graphite (HOPG) surface

STM image ~2x2 nm

2D FFT

0.34 nm

0.25 nm

0.14 nm
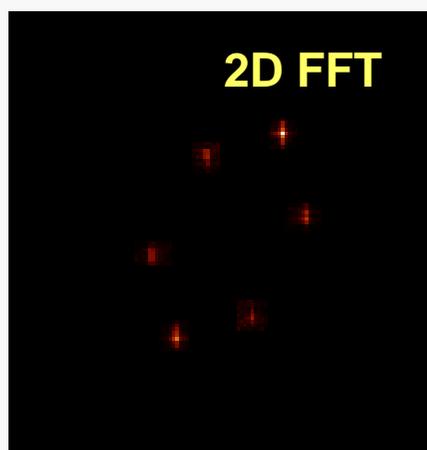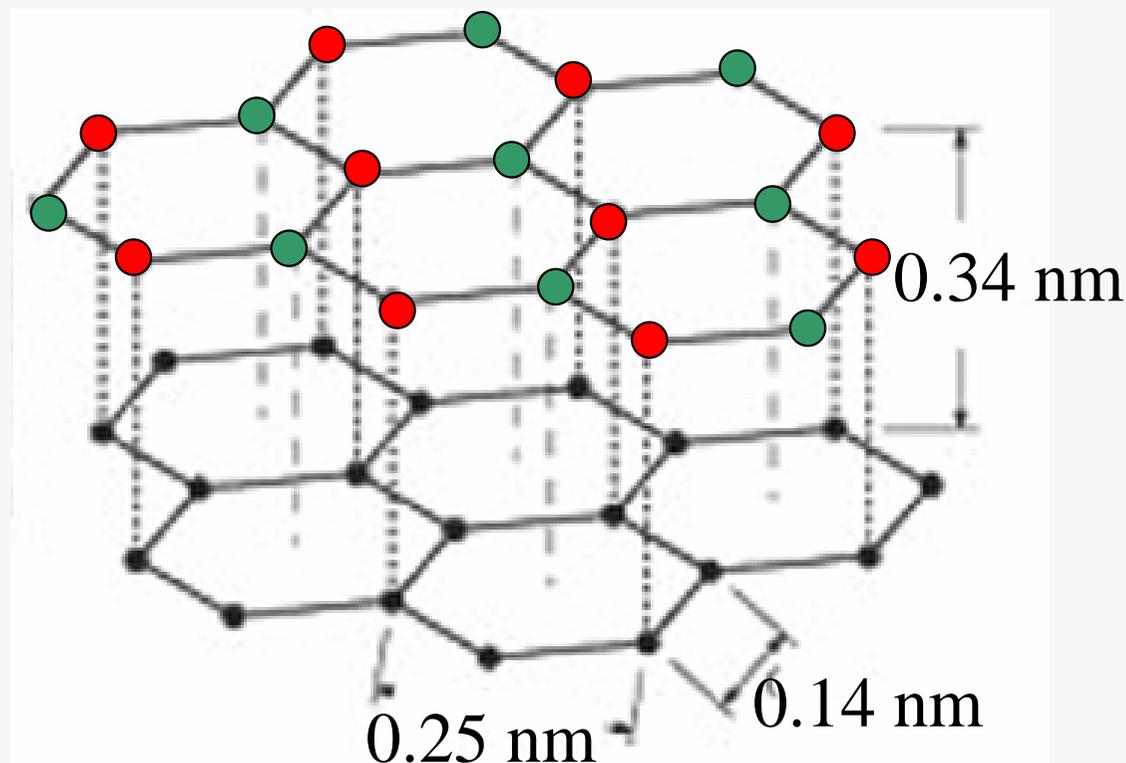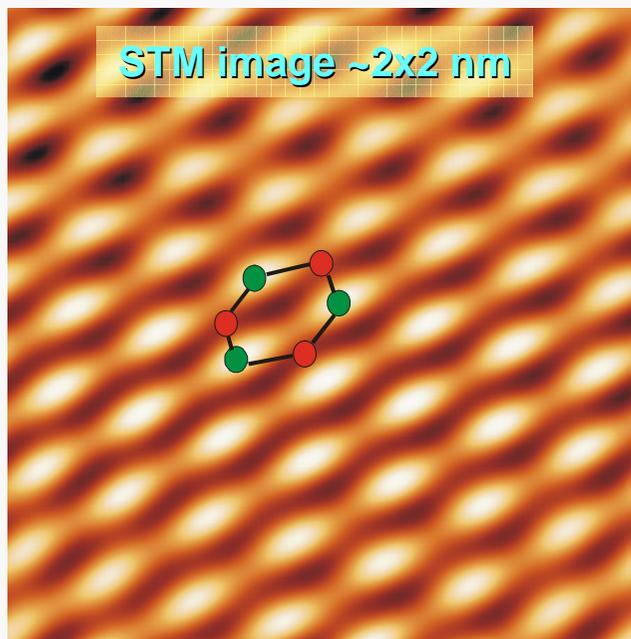
Two different positions of the carbon atoms in the graphite crystal lattice are possible: one with a neighbouring atom in the plane below (red) and one without a neighbour in the lattice below (green).

Consequently the electrical conductivity of the graphite surface varies locally slightly (different electronic density of states) so that the atoms without neighbours appear "higher" than the others (see e.g. I.P. Batra et al. Surf Sci 181 (1987) 126). This also causes the lattice constant between the bright 'hills' to have the higher value of 0.25nm than the nearest neighbour distance in the graphite lattice of 0.14nm.

Figure 4: Examples of CNTs with different circumference vectors C_h [5].

(5,5) armchair

(9,0) zig-zag

(10,5) chiral

STM

DOS
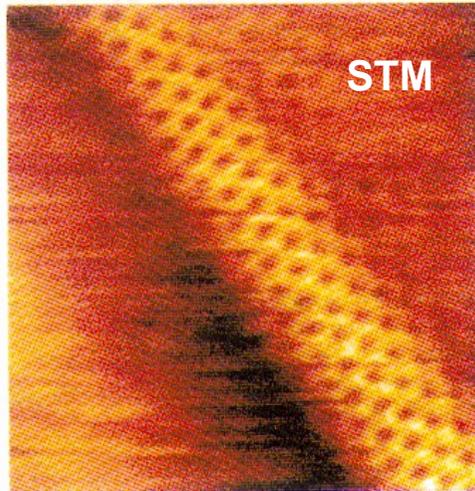
Figure 5: STM image at 77 K of a SWNT at the surface of a rope [6].

Da R. Waser Ed., Nanoelectronics and information technology (Wiley-VCH, 2003)

2.1 Geometrical Structure

The structure of CNTs is described by the circumference vector or **chiral vector C_h**, which represents the full circumference of the tube. It is defined by

$$C_h = na_1 + ma_2 \qquad (1)$$

where a_1 and a_2 are the unit vectors in the hexagonal lattice, and n and m are integers (Figure 1). C_h also defines the propagation vector P_h representing the periodicity of the tube parallel to the tube axis. Furthermore, it settles the so-called chiral angle which is the angle between C_h and a_1. If either n or m are zero, the chiral angle is $0°$ and the structure is called *zig-zag*. If $n = m$, the chiral angle is $30°$ and the structure is called *armchair* (Figure 4). All other nanotubes show chiral angles between $0°$ and $30°$. They are known as *chiral* nanotubes because they produce a mirror image of their structure upon an exchange of n and m.

Experimentally, the diameter of nanotubes is frequently determined by TEM, STM or AFM. The chiral structure can be determined by STM (Figure 5).
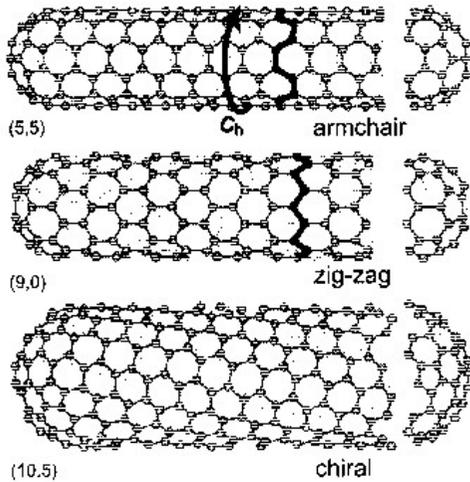
2.2 Electronic Structure of Graphene

For the discussion of the electronic structure of CNTs, we start again with graphene. As an extension of the description of fused benzene (Chap. 5), in graphene, a bonding π-band and an anti-bonding π^*-band is formed from the overlap between $2p_z$-AOs of adjacent atoms. P. R. Wallace [7] derived an expression for the 2-D energy states, W_{2D}, of the π-electrons in the graphene plane as a function of the wave vectors k_x and k_y (see also [8]):

$$W_{2D}(k_x, k_y) = \pm \gamma_0 \left[1 + 4\cos\left(\frac{\sqrt{3}k_x a}{2}\right)\cos\left(\frac{k_y a}{2}\right) + 4\cos^2\left(\frac{k_y a}{2}\right) \right]^{1/2} \qquad (2)$$

where γ_0 denotes the nearest-neighbour overlap (or: transfer) integral and $a = 0.246$ nm is the in-plane lattice constant. The two different signs in Eq. (2) represent the π- and π^*-band. The calculations show that the π- and π^*-band just touch each other at the corners of the 2-D Brillouin zone (Figure 6). In the vicinity of the Γ point, the dispersion relation is parabolically shaped, while towards the corners (K points) it shows a linear $W(k)$ dependence. At $T = 0$ K, the π-band is completely filled with electrons and the π^*-band is empty. Because the bands only touch at the K points, integration over the Fermi surface (which is a line for a two-dimensional system) results in a vanishing density of states. On the other hand no energy gap exists in the graphene dispersion relation. This means we are dealing with the unusual situation of a gapless semiconductor. (The real graphite yet is a metal since the bands overlap by approx. 40 meV due to the interaction of the graphene planes.)
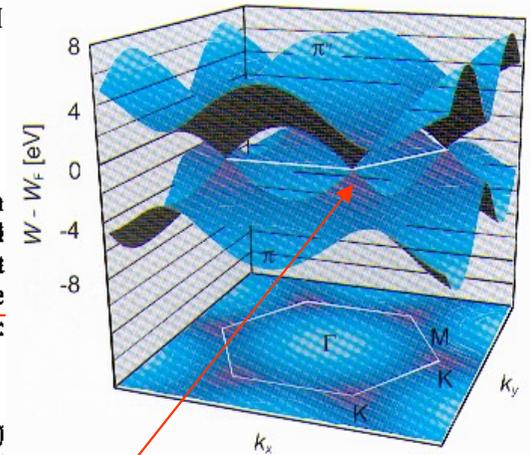

Figure 6: 3-D illustration of the dispersion relation of graphene.

Graphene: zero-gap semiconductor

Electronic structure of CNT II

2.3 Electronic Structure of Carbon Nanotubes

For the description of the band structure of graphene, it has been assumed that the graphene plane is infinite in two dimensions. For CNTs, we have a structure which is macroscopic along the tube axis, but the circumference is in atomic dimensions. Hence, while the density of allowed quantum mechanical states in axial direction will be high, the number of states in the circumferential direction will be very limited. More precisely, the roll-up by the chiral vector C_h leads to periodic boundary conditions in the circumferential direction. Quantum mechanically, these boundary conditions define allowed modes (1-D states) along the tube axis according to:

$$C_h \cdot k = 2\pi j \quad \text{with} \quad |j| = 0, 1, 2, \ldots$$

In the case of arm-chair tubes, the periodic boundary condition yield allowed values for the wave vector in circumferential direction according to:

$$k_{y,j} = \frac{j}{q_y} \frac{2\pi}{\sqrt{3}a}$$

where $q_y = n = m$. For the armchair geometry, the tube axis is identical to the x-direction and the circumference represents the y-direction. As an example of an armchair tube, Figure 7 shows the dispersion relation, the projection of the allowed 1-D states onto the first Brillouin zone of graphene, as well as the $W(k_x)$ relation for a (3,3) tube. Due to the periodic boundary conditions, i. e. by inserting Eq. (4) into Eq. (2), the allowed states condense into lines (black lines in Figure 7a). Here, there are $q_y = 3$ lines on either side of the center of the Brillouin zone and an additional line going through the center. In case of a (3,3) tube the allowed states include the K points. Since the system is now one-dimensional in an electronic sense, different from the case of graphene, the integration over the Fermi surface (which is the sum over the Fermi points) yields a finite density of states at the Fermi energy. The (3,3) tube, and armchair tubes in general, show a metallic behaviour.

DOS and geometry CNT

Armchair CNT

> **Periodic boundary conditions in armchair CNT affect the DOS**
>
> **Electronic configuration for armchair CNT indicate superposition of valence and conduction bands**
>
> **Transport properties are that of a conductor**

Figure 7: Dispersion relation of a (3,3) CNT.
(a) 3-D illustration of the dispersion relation for graphene including the allowed states for the (3,3) CNT. The periodic boundary conditions along the circumference of the tube result in a discrete set of allowed k_y values.
(b) Projection of the allowed states onto the first Brillouin zone of graphene. Obviously, the K points are allowed states for CNTs of this chirality.
(c) 2-D illustration of the dispersion $W(k_x)$. The states at the Fermi level indicate the metallic behaviour of this tube. The periodicity volume in the k-space is given by the interval from $-\pi/P$ to $+\pi/P$.
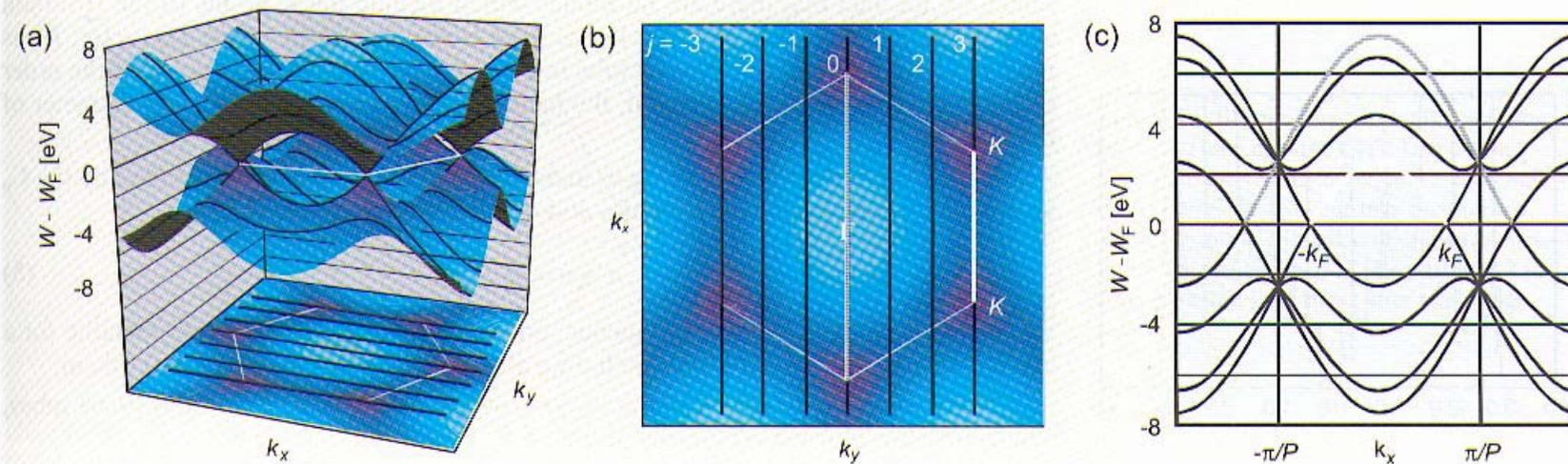
As an example of a chiral tube, Figure 8 shows the dispersion relation, the projection of the allowed 1-D states onto the first Brillouin zone of graphene, as well as the $W(k_x)$ relation for a (4,2) tube. We will illustrate why the electronic properties of this (4,2) tube is very different from the (3,3) tube despite their very similar diameters. Again, due to the periodic boundary conditions, the allowed states condense into lines (black lines in Figure 8a). In contrast to the (3,3) tube, the C_h vector is not parallel to the y-direction and, hence, leads to a mixed quantization of k_x and k_y. The propagation of an electron along the tube axis is described by a combination of of k_x- and k_y-components. For this reason, the general letter k is used in Figure 8c, representing the momentum of the electron in the direction of propagation. The band structure of (4,2) tubes is determined by the fact that there are no modes which include the K points of the Brillouin zone of graphene (Figure 8b). The Fermi level is not dependent on the C_h vector, W_F is now in a bandgap, i. e. this type of tube is a *semiconductor*. The bandgap is of the order of a few eV (Figure 8c). In general, the bandgap decreases with increasing diameter of the tube.

Chiral CNT

In general, the semiconducting or metallic behavior of CNTs is controlled by the C_h vector and, hence, by the relation of n and m. Metallic behavior occurs for

$$n - m = 3q \qquad (5)$$

Metal/semi

where q is an integer. As a consequence, one-third of all CNTs types are metallic for a statistic distribution of chiralities including all armchair types, since $q = 0$ for them.

The periodic boundary conditions for zig-zag tubes, $(n,0)$ tubes and $(0,m)$ tubes, results in allowed wave vectors according to

$$k_{x,j} = \frac{j}{q_x}\frac{2\pi}{a} \qquad (6)$$

The condition for metallic tubes, Eq. (5), is fulfilled for one-third of the tubes, i. e. if n or m are multiples of three. Figure 9 illustrates the density of state (DOS) for two zig-zag type CNTs [9], a (10,0) tube showing a bandgap and, hence, semiconducting behavior (Figure 9a), and a (9,0) tube showing no bandgap and, hence, metallic behavior (Figure 9b).

The discussion so far has been restricted to isolated SWNTs. Theoretical and experimental studies have shown that the intertube coupling within MWNTs and ropes of SWNTs [10], [11] have a relatively small effect on the band structure of a tube [12]. As a consequence, semiconducting and metallic tubes retain their character if they are a part of MWNTs or ropes. By statistical probability, most of the MWNTs and ropes show an overall metallic behavior, because one single metallic tube is sufficient to short-circuit all semiconducting tubes.

SWNT/MWNT

Periodic boundary conditions depend on the chirality

Electronic behavior depends on the structure:

➢ **armchair (n, n) are conductive**
➢ **n – m = 3i (i integer) are semi-metal**
➢ **otherwise, semiconductor**
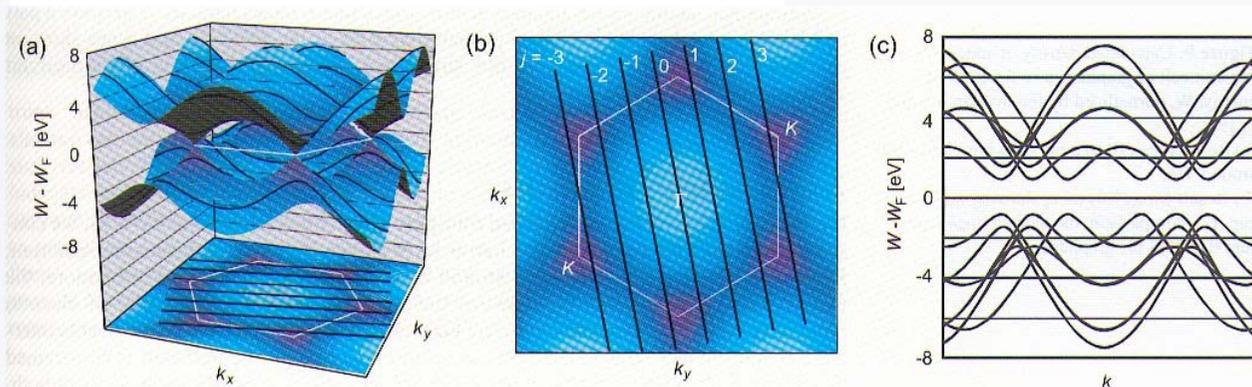
Figure 8: Dispersion relation of a (4,2) CNT.
(a) 3-D illustration of the dispersion relation for graphene including the allowed states for the (4,2) CNT. The periodic boundary conditions along the circumference of the tube result in a discrete set of allowed k values.
(b) Projection of the allowed states onto the first Brillouin zone of graphene. Obviously, the K points are no allowed states for CNTs of this chirality.
(c) 2-D illustration of the dispersion $W(k)$. the conduction band and the valence band are separated by a bandgap.

Resume of electronic properties in CNT

E

B_V

E_{Fermi}

B_C

Metallic CNT

Armchair (n,n)

Semimetallic CNT

m-n=3·i

Semiconducting CNT

m-n≠3·i
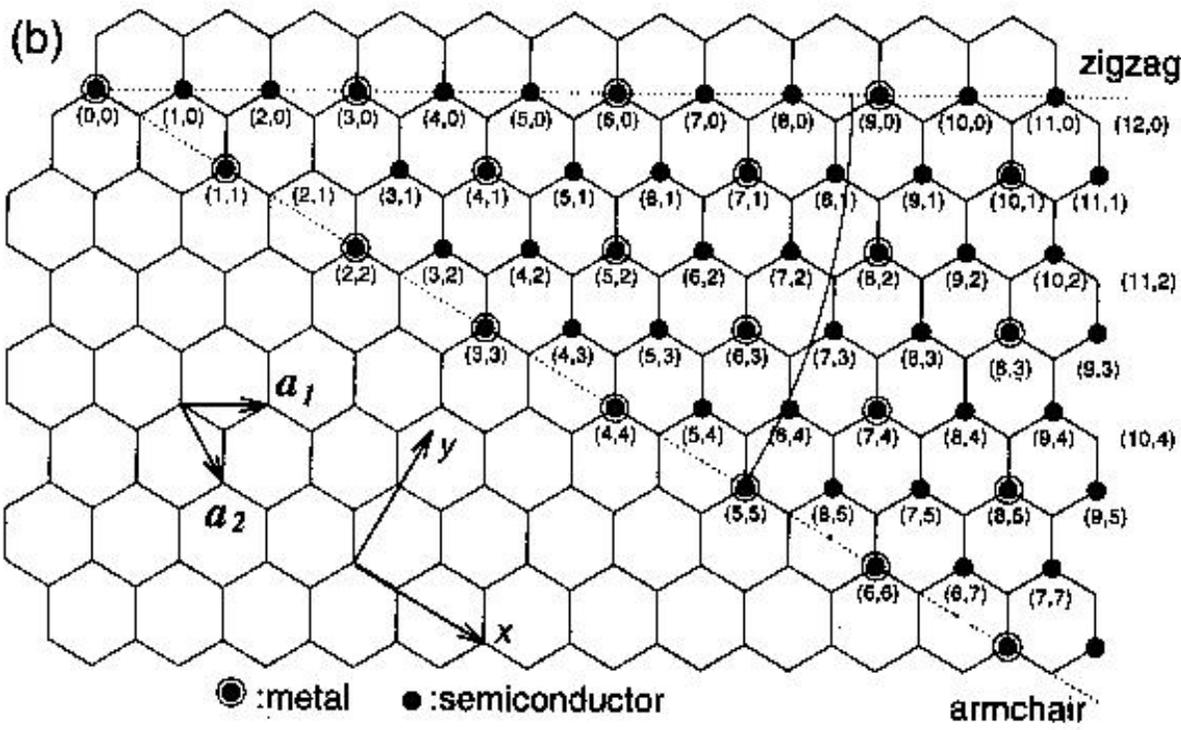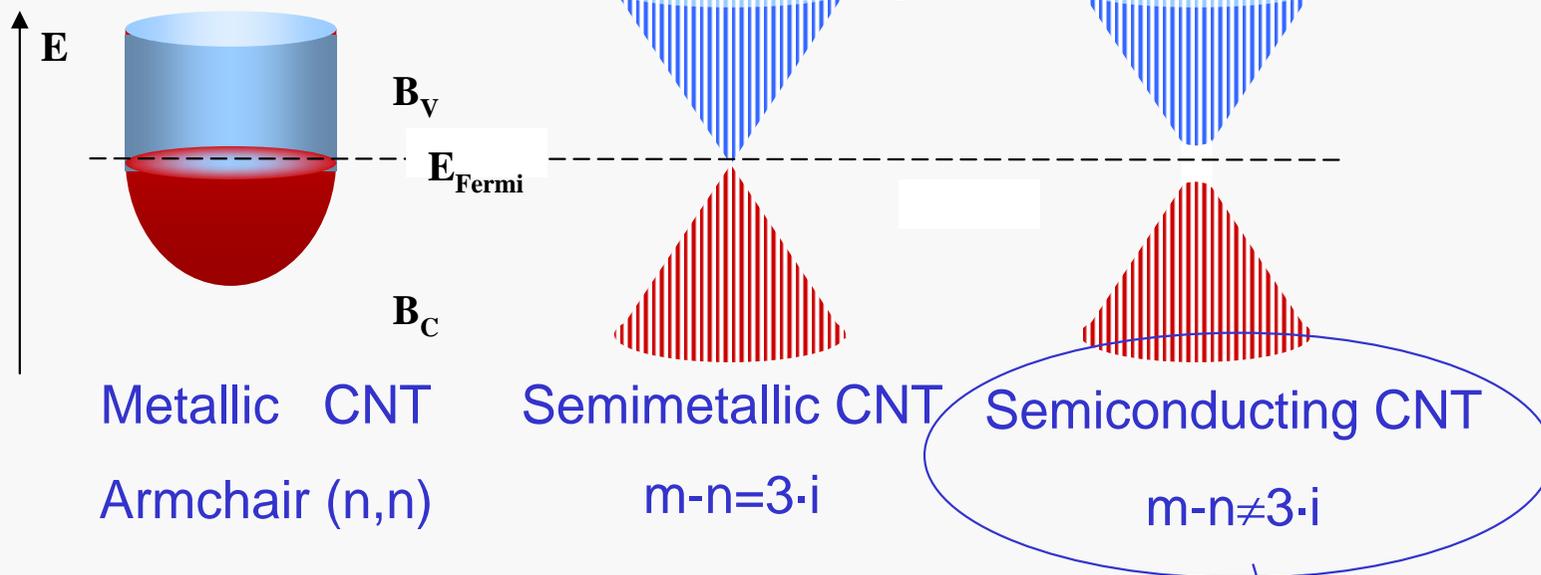
Tuneable band gap (2x10⁻³-1.1eV)

– E_g~1/d_{NT} also affected by:
chemical doping (B, N, O, Li, K…)

point defects (pentagons, heptagons)

(b)

zigzag

(0,0) (1,0) (2,0) (3,0) (4,0) (5,0) (6,0) (7,0) (8,0) (9,0) (10,0) (11,0) (12,0)

(1,1) (2,1) (3,1) (4,1) (5,1) (6,1) (7,1) (8,1) (9,1) (10,1) (11,1)

(2,2) (3,2) (4,2) (5,2) (6,2) (7,2) (8,2) (9,2) (10,2) (11,2)

(3,3) (4,3) (5,3) (6,3) (7,3) (8,3) (8,3) (9,3)

a_1

y

(4,4) (5,4) (6,4) (7,4) (8,4) (9,4) (10,4)

a_2

(5,5) (6,5) (7,5) (8,5) (9,5)

x

(6,6) (6,7) (7,7)

⊙ :metal   ● :semiconductor

armchair

For the discussion of the unperturbed transport of electrons in metallic SWNTs, we consider again the situation near the Fermi level shown by the 1-D dispersion spectrum, Figure 7c. The dispersion relation around the Fermi energy is linear. Furthermore, the energetical seperation, ΔW_{mod} between the modes at $\pm k_F$ is of the order of electron volts. It is this large energetical spacing between the 1-D subbands which prevents interband scattering to a large extend even at room-temperature. The transport is constrained to a single 1-D mode. Since there are subbands with positive and negative slope at both, $+k_F$ as well as for $-k_F$, one expects a Landauer conductance

Ballistic (1D)

$$G = 2 \cdot 2 \cdot \frac{e^2}{h} = \frac{4e^2}{h} \qquad (7)$$

for an ideal, scattering-free i. e. **ballistic transport** of a metallic CNT. The degeneracy due to the spin is considered by a factor 2.

According to different authors (e.g. [49]) it is expected that ballistic transport properties are maintained in carbon nanotubes over distances of several micrometers. For transport on a larger scale scattering has to be taken into account.

We will first consider the elastic **scattering at impurities**. For 3-D metals, the probability of a scattering event, i. e. the scattering rate, is described by the classical Rutherford scattering theory:

Scattering at impurities

$$\tau_{imp}^{-1} \propto v_F \cdot \frac{1}{v_F^4} = v_F^{-3} \qquad (8)$$

where v_F denotes the Fermi velocity. In particular, τ_{imp}^{-1} is independent of temperature. This result relies on the fact that the velocity of electrons in an interval of approx. $4 k_B T$ around the Fermi energy is given by v_F in a very good approximation. This is in general a valid assumption for 3-D metals where W_F is large compared to $k_B T$. Eq. (8) holds exactly, if the dispersion relation is linear within the energy interval of approx. $4 k_B T$. This condition is fulfilled for CNTs up to room temperature and above. Figure 10 is a magnification of Figure 7c and shows the segment of the dispersion relation in the vicinity of the Fermi positions at $\pm k_F$. The arrows indicate the Fermi velocities of the elec-

trons. Scattering at an impurity is an elastic scattering process. Consequently, an electron can only be scattered in another state at the *same* energy of the nanotube dispersion relation. The allowed final states for an electron in an initial state at position 1 are indicated as 2 to 4 in Figure 10. The change in electron momentum is accounted for by the impurities. Because of the one-dimensionality of the system small-angle scattering as present in 2-D or 3-D metals does not exist in carbon nanotubes. While scattering from 1 to 3 represents a forward scattering event without effect on the sample conductance, scattering from 1 to 2 or 4 is a backscattering event and will increase the CNT resistance. The two-terminal resistance of a CNT segment of length L will be

$$R_{imp} = \frac{h}{4e^2} \cdot \frac{L}{\lambda_{imp}} \qquad (9)$$

where λ_{imp} is the elastic mean free path which is roughly speaking the average distance between impurity centers. R_{imp} will be temperature independent in a good approximation.

Scattering at phonons

For the discussion of the **phonon scattering** of electrons on CNTs, we have to distinguish scattering by optical and acoustical phonons. Starting point for describing the latter is the linear dispersion of the *acoustical phonons* with $W_{ph} = \hbar c_{ph} k_{ph}$ [13]. Since the velocity of sound, c_{ph}, is approx. 10^4 m/s, i.e. about two orders of magnitude smaller than the Fermi velocity of the electrons ($v_F \cong 10^6$ m/s), the scattering of an electron by an acoustic phonon results in a rather small electron energy change. Figure 11 illustrates a possible final state 2 for an electron scattered by an acoustic phonon from an initial state 1. The two states are connected through a line with a slope (c_{ph}) much smaller than the one of the electron dispersion relation reflecting the aforementioned difference in velocities. Scattering from the crossed dispersion region around $+k_F$ to $-k_F$ is suppressed because there are no empty, allowed states available around $-k_F$ even at room-temperature. This can be understood as follows: Scattering from $+k_F$ to $-k_F$ requires a Δk of approximately $2 k_F$ which has to be delivered by the phonon. This means $k_{ph} = \Delta k = 2 k_F$. The corresponding phonon energy is $W_{ph} = \hbar c_{ph} k_{ph} \cong 100$ meV. This value is much higher than $k_B T$ even at room-temperature and thus scattering from around $+k_F$ to $-k_F$ is suppressed. On the other hand, scattering from 1 to 2 remains possible even at lowest temperatures. This is true because the required energy transfer W_{ph} is always smaller than the electrical excess energy of the electron in position 1, since $c_{ph} \ll v_F$.
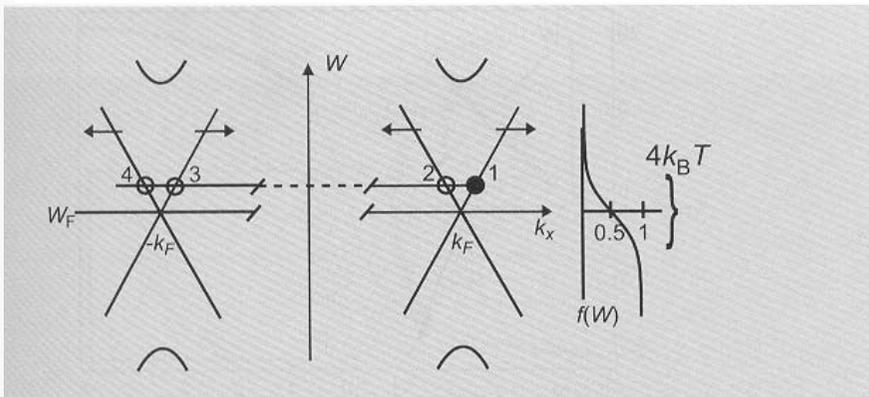
Figure 10: Illustration of impurity scattering processes on a metallic CNT. Dispersion relation in the vicinity of $-k_F$ and $+k_F$ as well as the Fermi-Dirac occupancy relation are shown. Position 1 (black circle) indicates an initial state of an electron, the positions 2 to 4 are potential final states after scattering events.

A quantitative expression for the temperature dependence of the acoustical phonon scattering can be derived from a consideration of the dimensions. Since the Debye temperature of CNT is approx. 2000 K [14], the situation for T < 300 K is described by the Grüneisen relation. For 3-D metals, this is a dependence of the scattering rate according to

$$\tau_{\mathrm{ph}}^{-1} \propto T^5 \qquad (10)$$

This temperature dependence is composed of three factors. A first $\propto T^2$ dependence results from the density of phonon states in three dimensions. A second $\propto T^2$ term describes the small-angle scattering in 3-D metals. And finally, there is factor $\propto T$ from the energy transfer between electron and phonon. For 1-D systems such as CNTs, the first two terms have to be changed to $\propto T^0$, because the 1-D phonon DOS shows no temperature dependence and the small-angle scattering is not allowed in 1-D structures. The final $\propto T$ term remains and, hence, the resistance contribution due to acoustical phonon is given by

$$R_{\mathrm{ph}} = \frac{h}{4e^2} \cdot \frac{L}{\lambda_{\mathrm{ph}}} \quad \text{where} \quad \lambda_{\mathrm{ph}} = v_{\mathrm{F}} \cdot \tau_{\mathrm{ph}} \text{ and} \quad \tau_{\mathrm{ph}} \propto T^{-1} \qquad (11)$$

For small electric excess energies of the electrons (approx. eV < 100 meV), scattering by optical phonons can be neglected since there are no unoccupied states at energies

$$W_{\mathrm{final}} = W_{\mathrm{initial}} - W_{\mathrm{opt}} \qquad (12)$$

where W_{opt} denotes the energy of optical phonons [14]. For large dc biases, i. e. high fields, electrons on the CNT are taking up energies well beyond values of $k_{\mathrm{B}}T$, they become *hot*. Interestingly, hot in this case does not mean that the electron velocity has increased. Because of the special situation of a linear dispersion relation, the velocity of the carriers remains constant while their energy increases. This changes the situation completely. In the case of hot electrons, scattering by *optical phonons* can be the main contribution to the overall resistance of CNTs. Figure 12 shows the high-field *I-V* characteristics of metallic CNTs at different temperatures. The curves overlap almost completely, proving a temperature independent behavior. For small voltages, approx. V < 0.2 V, the *I-V* characteristics exhibits a linear behavior. For larger voltages, the *I-V* curve is strongly non-linear. For voltages approx. > 5 V, the current exceeds 20 μA which corresponds to a current density of more than 10^9 A/cm². Furthermore, it seems that a saturation current I_0 is approached at large bias. The resistance shows a constant value R_0 at small bias and increases linearly for V > 0.2 V (see right inset in Figure 12), i.e. it can be expressed by:

$$R = R_0 + V / I_0 \qquad (13)$$

This behaviour can be explained by the inset picture in the left of Figure 12. Once an electron has gained enough energy to emit an optical phonon, it is immediately backscattered [15]. A steady state is approached in which the electrons moving in forward direction have an energy W_{opt} higher than the backward moving ones. This leads to a saturation current

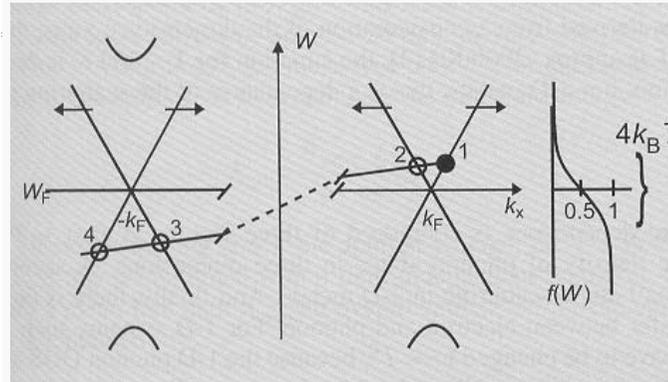$$I_0 = \frac{4e^2}{h} \cdot \frac{W_{\mathrm{opt}}}{e} \qquad (14)$$

Figure 11: Illustration of an acoustic phonon scattering event on a metallic CNT. Dispersion relation in the vicinity of $+k_{\mathrm{F}}$ as well as the Fermi-Dirac occupancy relation are shown. Position 1 (black circle) indicates an initial state of an electron, position 2 is the final state after the scattering event.

Here, the first term on the right represents the Landauer conductance as before and the second the voltage corresponding to W_{opt}. Using a value of approx. 160 meV [14], Eq. (14) leads to a saturation current of approx. 25 mA, in very good agreement with the experimental results. Accordingly, the mean free path l_{opt} for backscattering phonons is just the distance an electron needs to accumulate the threshold energy:

Scattering at optical phonons

$$\lambda_{\mathrm{opt}} = \frac{W_{\mathrm{opt}}}{e} \cdot \frac{L}{V} \qquad (15)$$

L denotes the electrode spacing and V the applied voltage, i.e. V/L is the electric field along the CNT. If this is combined with a field-independent scattering term (i. e. from impurities) with a mean free path λ_{imp}, an overall expression for the voltage dependent resistance can be obtained:

$$R = \frac{h}{4e^2} \cdot L \left(\frac{1}{\lambda_{\mathrm{imp}}} + \frac{1}{\lambda_{\mathrm{opt}}} \right) = \frac{hL}{4e^2 \lambda_{\mathrm{imp}}} + \frac{h}{4eW_{\mathrm{opt}}} \cdot V \qquad (16)$$

The right equation is obtained by inserting Eq. (15) into the expression for λ_{opt}. Eq. (16) fully explains the empirical result, Eq. (13).

Scattering processes must be duly accounted for

An additional mechanism that leads to a resistance contribution is the **electron-electron scattering**; a mechanism which may get especially pronounced in 1-D conductors. Typically, electron-electron scattering does not result in any measurable change in resistance for a normal conductor. This is true because energy and momentum conservation can only be fulfilled if as many electrons are backscattered as get scattered in the forward direction. The situation is drastically changed for a carbon nanotube. Figure 13 shows the dispersion relation in the vicinity of k_F. Because of the mode crossing, two electrons in the positions 1 and 1′, which contribute to the forward transport, may get scattered in positions 2 and 2′, respectively. The total energy and momentum is conserved during this process. The scattered electrons in 2 and 2′ now occupy states in the negative current direction. Hence, this process leads to a resistance increase. With raising temperature, the number of allowed initial and final states increases and so does the scattering probability. A detailed analysis [16] reveals a linear dependence of the electron-electron scattering rate on the temperature:

$$R_{e-e} = \frac{h}{4e^2} \cdot \frac{L}{\lambda_{e-e}} \quad \text{with} \quad \tau_{e-e} \propto T^{-1} \tag{17}$$

where λ_{e-e} is the mean free path between scattering events and τ_{e-e} is the inverse scattering rate. The scattering rate also rises with increasing electric excess energies, eV, of the electrons because the number of allowed states increases.

Transport in metallic CNT ruled by 1D geometry

Ballistic transport with scattering effects

Figure 12: High-field I-V characteristics for metallic CNTs at different temperatures. The right inset plots $V/I = R$ vs. V. The left inset shows a section of the dispersion relation and illustrates the phonon emission [14].
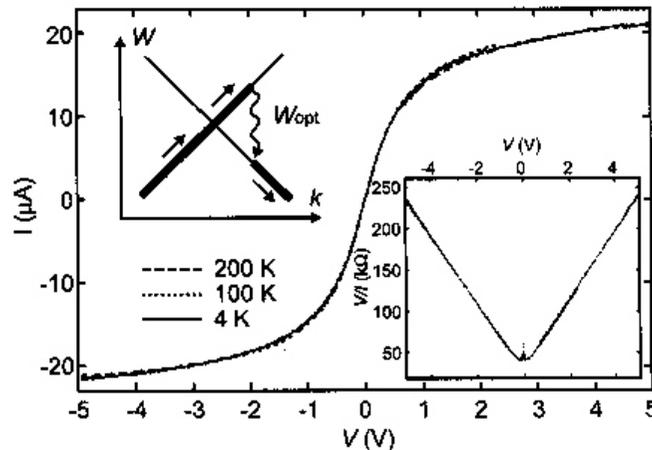
Metallic behavior observed with contribution from contact resistance
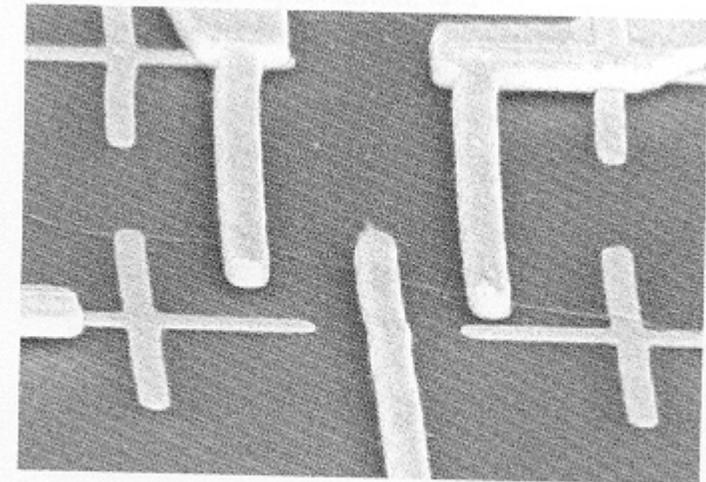
Figure 14: SEM image of a rope of single-wall nanotubes contacted by several gold fingers attached to the top of the tube.

4 Carbon Nanotube Interconnects

The lateral scaling of dimensions in silicon technology affects the transistors as well as their interconnects. In modern technology generations, chip wiring is produced using the damascene technique, where grooves are etched into a dielectric layer and subsequently filled with copper. Chemical mechanical polishing is used to remove the excess copper above the grooves. The result resembles inlay work or the patterned structure on a damascene sword which lends its name to the technique (see Chap. 29).

Scaling the width of the lines increases the resistance, not only because of the reduced cross section, but also due to increased scattering from the surface and the grain boundaries [45]. This problem can not be addressed by material innovation because the only metal with better bulk conductivity than copper is silver with only a 10 % improvement. If, however, wires could be made without intrinsic defects and with perfect surfaces, additional scattering might be avoided.

Carbon nanotubes may fulfill this requirements to a large extent. They offer unparalleled translational symmetry in one dimension with an intrinsically perfect surface. For metallic nanotubes the electron density is high and the conduction is easy along the tube axis due to the π-electron system. Moreover, it has been shown [49] that electron transport along the tubes is ballistic within the electron-phonon scattering length, which is of the order of micrometers at room temperature [17], [47] (Sec. 2.4). The absence of scattering also allows for much higher current densities than in metals.

Carbon nanotubes can be grown in different ways as described in Sec. 3. Most suitable for microelectronic applications is the catalyst mediated CVD growth [48]. This method can be used to grow CNTs at predefined locations if the catalyst is patterned by lithographic methods (Figure 18).
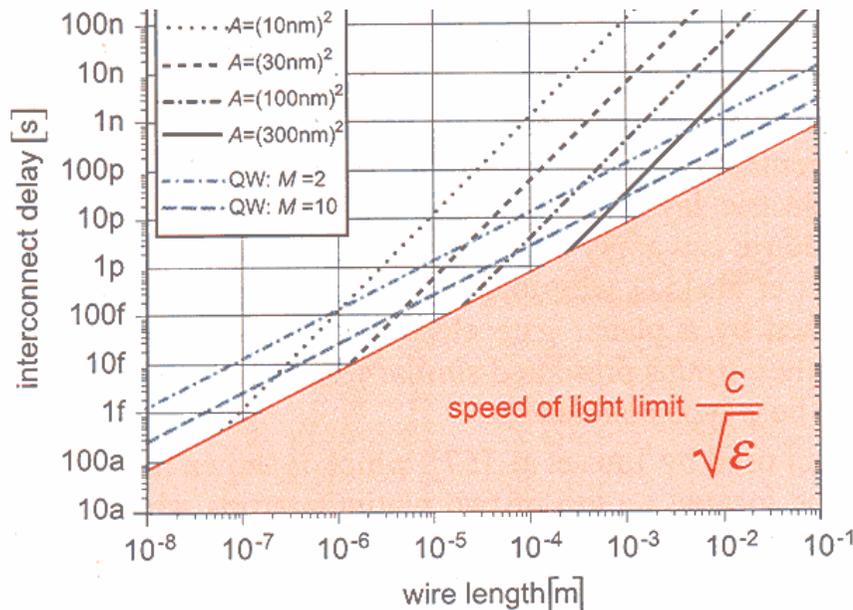
CNT ideally suited as (ballistic) interconnects

Lithographic patterning of catalysts can be useful to define the interconnected region

Figure 21: Signal delay in ohmic and ballistic wires as a function of wire length. The black lines represent the delays of ohmic wires with different cross sections A. Surface scattering has been taken into account. For wire lengths smaller than the intersections of black and red lines, the delay is governed by the speed of light and the relative permitivity of the dielectric. The nanotube wires display a completely different behavior to the ohmic wires, as shown by the blue lines. Due to the length-independent resistance, nanotubes exhibit better delay values for longer wires. M represents the number of conductive channels, that can be formed either by the number of occupied energy levels or by the number of shells of a multi-wall nanotube.
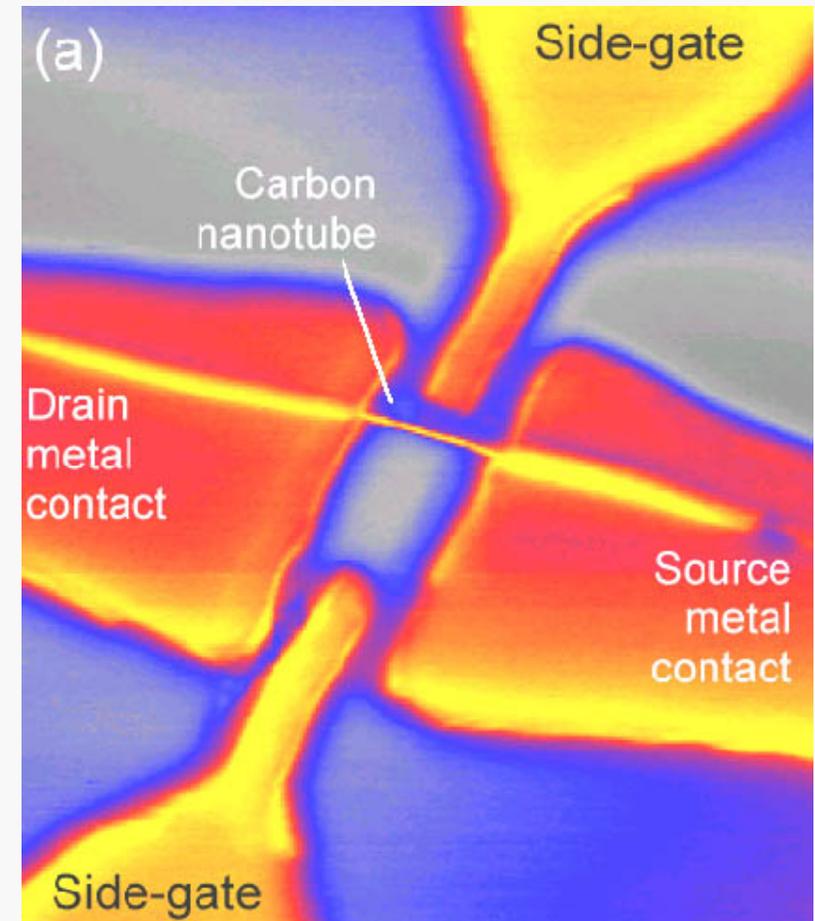
Active devices with CNT

5.1 Comparison to MOSFETs

The success of modern silicon technology is owed, to a large extent, to MOSFETs and the CMOS concept in which circuits draw current only during the switching action and are thus the indispensable ingredients for low power complex circuits like processors and controllers. The inversion channel of MOSFETs can be considered as a 2-D conduction system. Electron motion in the inversion channel is not *apriori* restricted in planes but due to high gate fields the motion perpendicular to the gate plane is quantized giving rise to subband formation. The conductive channel can be considered as a 2-D electron gas. At room temperature many subband levels contribute to the current transport enabling a high driving capability and switching speed.

Semiconducting carbon nanotubes can be operated in a gate electrode configuration in a similar way to silicon MOSFETs. The electronic properties of CNTs have been described in Sec. 2. The excess electrons are delocalized and form a highly conductive π-electron system. Unlike in silicon MOSFETs the electron system of a nanotube is 1-D. Placing a field electrode next to the nanotube one can influence its conductivity by the accumulation or depletion of electrons provided that the electron density is not to high (the tube is semiconducting). This configuration is called CNTFET in analogy to the silicon field effect transistor. As the electrical characteristics of carbon nanotubes strongly depend on their chirality, diameter and doping, the characteristics of CNTFETs can be controlled by choosing the appropriate morphology of the CNT. Single-wall semiconducting tubes are best suited for CNTFETs because their electron system is not bypassed by inner shells.

	p-type CNFET	Ref. 59	Ref. 60
Gate length (nm)	260	15	50
Gate oxide thickness (nm)	15	1.4	1.5
V_t (V)	−0.5	~ −0.1	~ −0.2
I_{ON} (μA/μm) ($V_{ds} = V_{gs} - V_t \approx$ -1 V)	2100	265	650
I_{OFF} (nA/μm)	150	< 500	9
Subthreshold slope (mV/dec)	130	~ 100	70
Transconductance (μS/μm)	2321	975	650

(a) Side-gate / Carbon nanotube / Drain metal contact / Source metal contact / Side-gate

CNTFET with appealing performance can be envisioned

Back-gate FET configuration

*The CNT lies on the contacts by chance*

CNT deposited from solution

Figure 25: A carbon nanotube field effect transistor (CNTFET). The nanotube (red) is located on top of two platinum contacts (yellow). The back-gate-stack (blue) is formed by a silicon dioxide dielectric on top of a silicon wafer (colored AFM-image taken from [57]).

source electrode
drain electrode
nanotube molecule

silicon oxide

silicon gate

*Semiconducting CNT selected a posteriori*
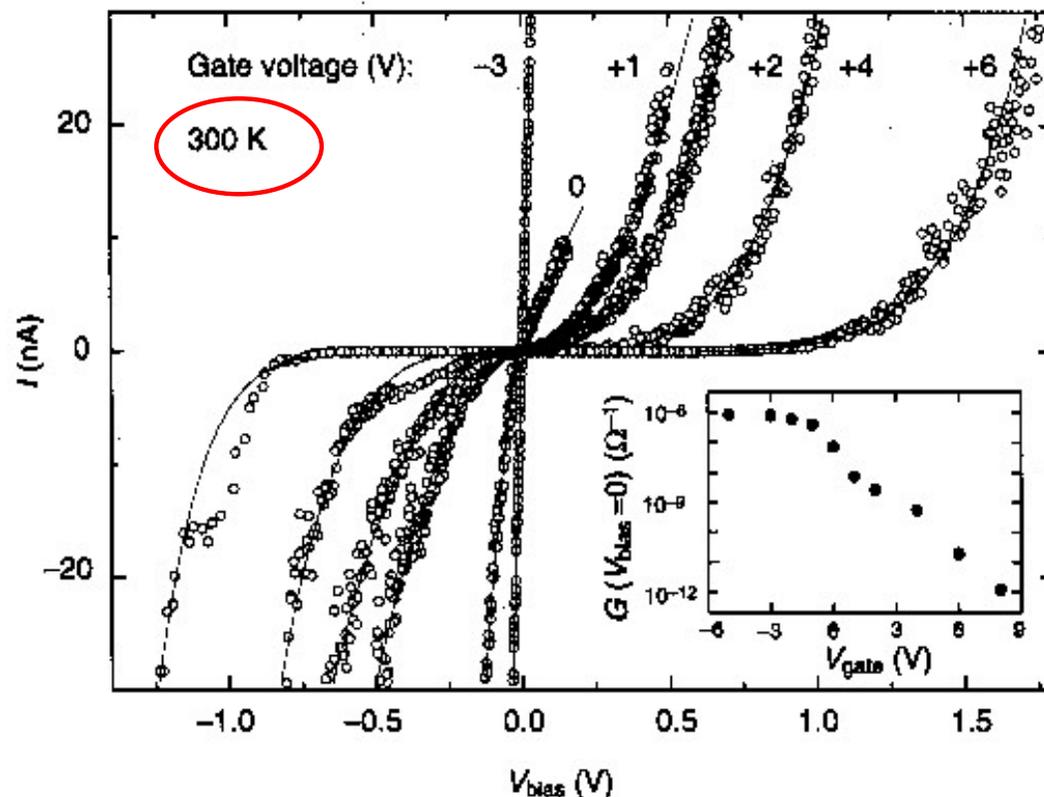
Figure 26: The current-voltage characteristics of a semiconducting single-wall carbon nanotube for different gate voltages (see Figure 25). For large positive gate voltages the conductance of the tube is very small for source-drain biases less than approximately 1 V. Changing the gate voltage to negative values increases the conductivity steadily until saturation is reached at approximately −3 V (see insert). The maximum conductivity is comparable to the values found for metallic tubes measured in the same experiment (taken from [57]).
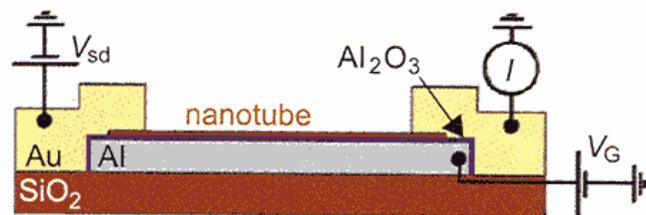
Tans et al., Nature 1998

Room temperature operation

Back-gate CNTFET II

Isolated back-gate FET configuration
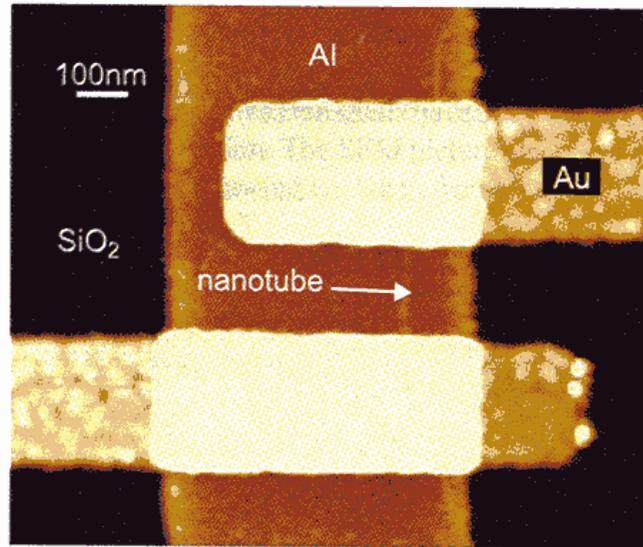

EBL + lift-off for the electrodes

Figure 28: Isolated back-gate CNTFET. The gate is realized by an Al-strip on top of SiO_2. The gate oxide is the naturally grown thin Al_2O_3 layer on top of the Al-strip. Source and drain contacts are made by Au deposition ([64]).

Wind et al., APL 2002

5.5 Isolated Back-Gate Devices

The CNT-devices discussed so far were controlled by a common back-gate stack which consists of a thermal oxide layer on top of a doped silicon wafer. Thus, the gate electrode extends over the whole silicon wafer and covers also the large contact pad areas. Due to the risk of defects resulting in high leakage currents or circuit shorts the gate oxide thickness must be kept in the 100 nm range. An effective gate control can therefore only be achieved with high gate voltages and the gain of most devices is smaller than unity. However, the Delft University group succeeded in constructing an isolated back-gate device by exploiting thin, naturally grown Al_2O_3 on top of a patterned aluminum electrode as gate oxide with a thickness of a few nanometers [64]. The basic device is displayed in Figure 28. Source and drain electrodes are patterned by electron-beam lithography and subsequent metal deposition and lift-off on top of a 1 nm diameter single-wall nanotube pre-selected and positioned by AFM.
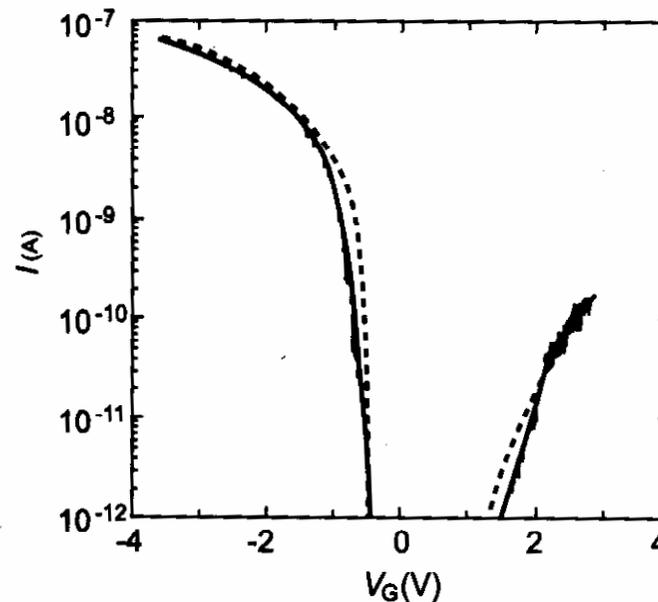
p and n channels can be opened (depending on the gate voltage)

Figure 29: Source-drain current of a single-wall nanotube on Al_2O_3 gate dielectric for a source-drain voltage of 5 mV. p- and n-channels can be opened by altering the gate voltage (after [64]).

Doping and complementary CNTFET

Complementary channels (i.e., n-type CNTFETs) can be achieved by alkali doping

Locally selective doping can be used to create the analogous of a pn junction (in CNT terms!)
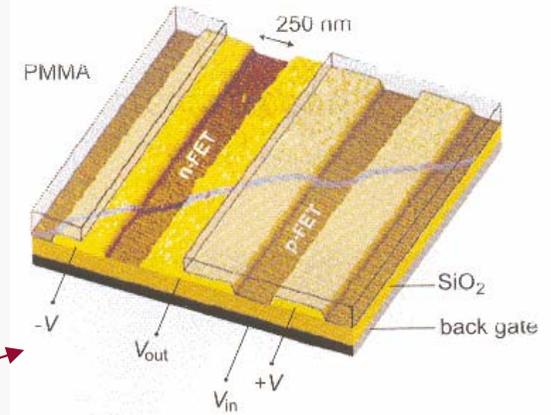

Figure 32: Intramolecular complementary CNTFET gate made by an n-type and p-type CNTFET in series, operated by a common back-gate. Complementary transistors are produced from one single nanotube by doping the section which is not covered by the PMMA resist with potassium (after [63]).
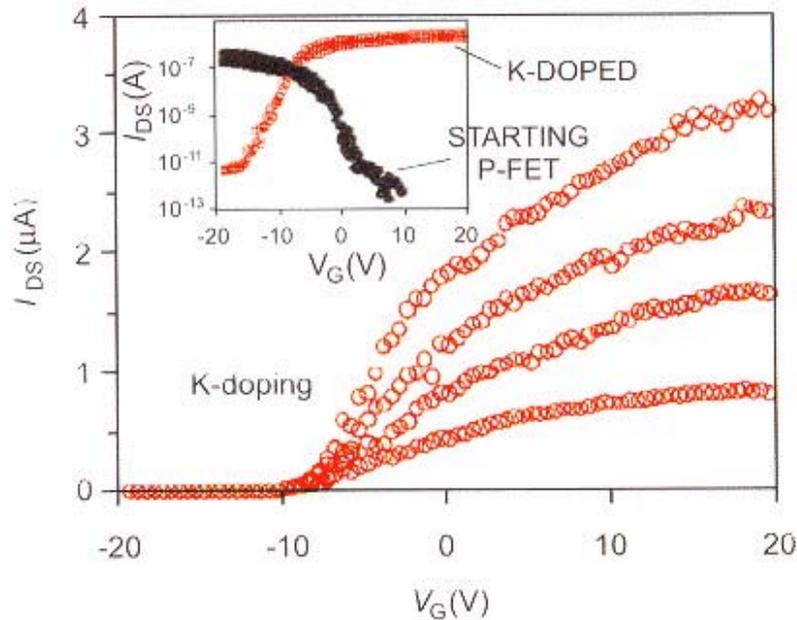

Figure 27: Inversion of the conductivity type of a semiconducting carbon nanotube. As displayed by the insert the starting device was a p-type CNT-FET. After exposure to potassium vapor, the conductivity type was reversed with current flowing for positive gate voltages (after [63]).
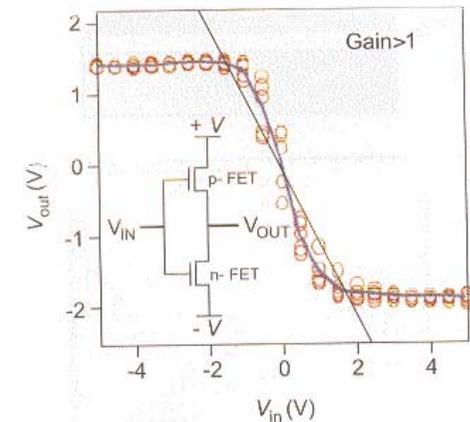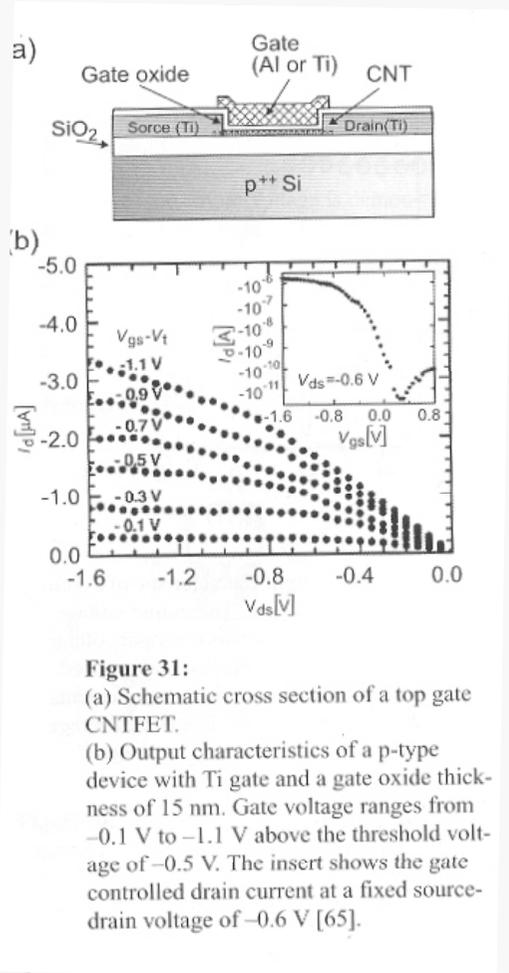

Figure 33: Input-output characteristic of a complementary CNTFET gate. The output voltage switches from logical 1 to 0 as the input voltage changes from negative to positive values. Red circles represent the data of five measurements on the same device. The blue line is the average of this measurements indicating a voltage gain > 1 (straight line).
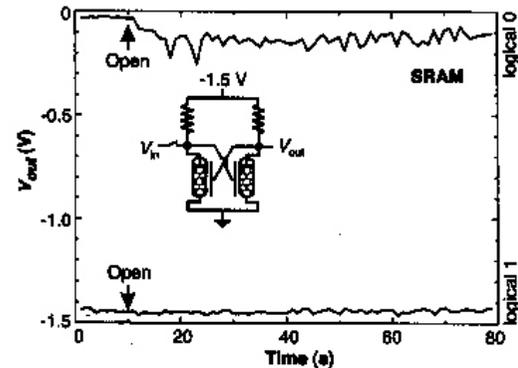
A freedom similar to what is common in conventional technology can be achieved (but for setting up the CNT position…)

Top-gate CNTFET and memories

Top-gate FET configuration

Figure 31:
(a) Schematic cross section of a top gate CNTFET.
(b) Output characteristics of a p-type device with Ti gate and a gate oxide thickness of 15 nm. Gate voltage ranges from −0.1 V to −1.1 V above the threshold voltage of −0.5 V. The insert shows the gate controlled drain current at a fixed source-drain voltage of −0.6 V [65].

Example of memory cell (based on digital electronics)

Figure 36: A simple SRAM cell made by two cross-coupled CNTFETs with external resistors. Writing either 1 or 0 to the input and disconnecting the input shows that the output remains in the stored state (taken from [64]).

Example of a futuristic memory device based on fullerene/CNT "switch"

Figure 39: A bucky ball incorporated in a short closed carbon nanotube (right). The Van der Waals forces favor two stable positions at both ends of the tube (left) which can be exploited for bit storage. The bucky ball is positively charged by the incorporation of a potassium ion (after [69]).
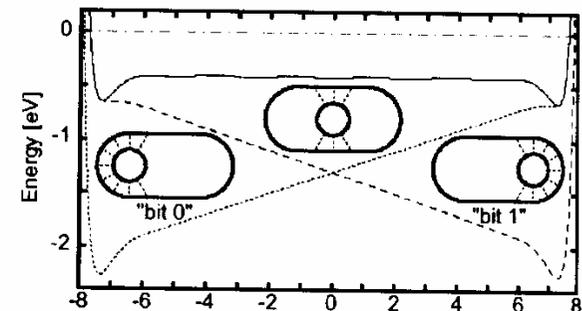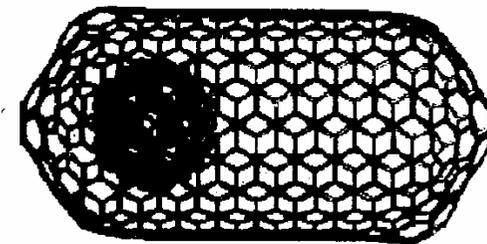
A new, unexplored range of potential applications are under investigation for CNT in the area of nanoelectronics

Conclusions

✓ Isolated nanoparticles play a relevant role in nanotechnology

✓ Cluster physics (and chemistry) is the basis for nanoparticle production and investigation

✓ Nanoparticle with linear geometry can have appealing potential exploitations (mostly thanks to their behavior, in between meso- and microscopic)

✓ A special class of nanoparticles is based on carbon (*and, maybe, on silicon*)

✓ Carbon nanotubes present a huge potential for applications in a very broad area, including nanoelectronics